

REPORT DOCUMENTATION PAGE				<i>Form Approved</i> <i>OMB No. 0704-0188</i>	
<small>The public reporting burden for this collection of information is estimated to average 1 hour per response, including the time for reviewing instructions, searching existing data sources, gathering and maintaining the data needed, and completing and reviewing the collection of information. Send comments regarding this burden estimate or any other aspect of this collection of information, including suggestions for reducing the burden, to the Department of Defense, Executive Services and Communications Directorate (0704-0188). Respondents should be aware that notwithstanding any other provision of law, no person shall be subject to any penalty for failing to comply with a collection of information if it does not display a currently valid OMB control number.</small>					
PLEASE DO NOT RETURN YOUR FORM TO THE ABOVE ORGANIZATION.					
1. REPORT DATE (DD-MM-YYYY)		2. REPORT TYPE		3. DATES COVERED (From - To)	
4. TITLE AND SUBTITLE				5a. CONTRACT NUMBER	
				5b. GRANT NUMBER	
				5c. PROGRAM ELEMENT NUMBER	
6. AUTHOR(S)				5d. PROJECT NUMBER	
				5e. TASK NUMBER	
				5f. WORK UNIT NUMBER	
7. PERFORMING ORGANIZATION NAME(S) AND ADDRESS(ES)				8. PERFORMING ORGANIZATION REPORT NUMBER	
9. SPONSORING/MONITORING AGENCY NAME(S) AND ADDRESS(ES)				10. SPONSOR/MONITOR'S ACRONYM(S)	
				11. SPONSOR/MONITOR'S REPORT NUMBER(S)	
12. DISTRIBUTION/AVAILABILITY STATEMENT					
13. SUPPLEMENTARY NOTES					
14. ABSTRACT					
15. SUBJECT TERMS					
16. SECURITY CLASSIFICATION OF:			17. LIMITATION OF ABSTRACT	18. NUMBER OF PAGES	19a. NAME OF RESPONSIBLE PERSON
a. REPORT	b. ABSTRACT	c. THIS PAGE			19b. TELEPHONE NUMBER (Include area code)

Atmospheric Propagation of High Energy Lasers: Modeling, Simulation, Tracking, and Control

AFOSR Grant F49620-02-01-0319

Final Report

Steve Gibson (PI)
Mechanical and Aerospace Engineering
University of California, Los Angeles 90095-1597
(310) 825-9362
gibson@ucla.edu

Investigators

Steve Gibson (PI) and T.-C. Tsao (Co-PI)

Mechanical and Aerospace Engineering
University of California, Los Angeles 90095-1597
gibson@ucla.edu, ttsao@seas.ucla.edu

Michael C. Roggemann and Timothy J. Schulz

Department of Electrical and Computer Engineering
Michigan Technological University
Houghton, Michigan 49931
mroggema@mtu.edu, schulz@mtu.edu

Allen Tannenbaum

School of Electrical and Computer Engineering
Georgia Institute of Technology
Atlanta, GA 30332-0250
allen.tannenbaum@bme.gatech.edu

Eric Magee and Matthew Whiteley

MZA Associates Corporation
1360 Technology Ct Ste 200
Dayton OH 45430-2211
emagee@mza.com, whiteley@mza.com

Eric Ben G. Fitzpatrick and Yun Wang

Tempest Technologies
Los Angeles, CA 90045
fitzpatrick@tempest-tech.com, wang@tempest-tech.com

Mikhail Belen'kii

Trex Enterprises Corporation
San Diego, CA 92121
mbelenkii@trexenterprises.com

Contents

1	Introduction	1
2	Adaptive Control of Laser Beams	3
3	HEL Propagation through Extended Turbulence	13
4	Novel Methods for Wavefront Sensing and Beam Control	18
5	Modeling and Simulation of HEL Wavefront Propagation	26
6	Active Contours for Tracking	43
A	Personnel Supported	51

Chapter 1

Introduction

Under this MRI funded by HEL JTO and AFOSR, UCLA, in collaboration with Michigan Tech, Georgia Tech, MZA Associates Corporation, Tempest Technologies, Trex Enterprises Corporation, ATK Mission Research and the Air Force Institute of Technology (AFIT), has established a comprehensive research program in high-performance control of high energy lasers (HEL), modeling and simulation of HEL, wavefront sensing, and target tracking. Under this program, researchers have developed adaptive filtering and control methods for wavefront prediction and correction and precise pointing of laser beams to compensate for the effects of atmospheric turbulence, platform vibration, target motion and sensor noise, all of which degrade the performance of laser weapons and communication systems.

Recent improvements in laser power and wave front control technology for space surveillance and laser anti-satellite and anti-ballistic missile weapons has motivated interest in extensions and alternative uses of this technology. Of particular interest are directed energy weapons, such as lasers. The agility and speed with which laser weapons can operate, combined with potential pinpoint accuracy and low collateral damage associated with these weapons make laser weapons highly desirable for a variety of applications, including high altitude Airborne Laser (ABL), low altitude tactical battlefield scenarios, and marine scenarios. However, considerable fundamental scientific work must be conducted to bring these weapons to the battlefield with the capability to deliver energy to the target through the atmosphere in each scenario of interest. Overcoming the technological barriers requires a multidisciplinary approach that combines research on the physics of beam propagation and control as well as on the mathematics and practical implementation of advance methods for active beam control and target tracking.

The research team for this multidisciplinary research initiative is making a comprehensive, integrated attack on the broad range of modeling and simulation, beam control, and target tracking problems that must be solved to achieve the potential of high energy laser systems. This report discusses the main results of the research.

Members of our team have worked in close collaboration so that each group can take advantage of the expertise in the other groups. The modeling and simulation research has been conducted by Michigan Tech, MZA Associates Corporation, ATK Mission Research, Tempest Technologies, and Trex Enterprises. Independent modeling investigations have been performed by these member groups, with insights from all influencing the wave-optics propagation models developed by MZA Associates Corporation for high-fidelity simulation of directed-energy weapons systems. The MZA codes have been used extensively by UCLA, Georgia Tech, and Tempest Technologies for investigation of the problems of adaptive optics and target tracking. Thermal blooming models developed by Trex Enterprises have been incorporated in MZA's simulations so that the team members can develop adaptive optics methods and image processing methods to mitigate the effects of thermal blooming on beam control and tracking. Also, we have investigated the integration of the novel

wavefront sensing methods being developed at Michigan Tech with the new methods for adaptive optics being developed at UCLA and Tempest Technologies.

New methods for correcting wavefront errors have been developed at UCLA, Tempest Technologies, Michigan Tech, and Trex. The effort on image processing methods for tracking through turbulence, the primary achievement of which has been the Bayesian tracking algorithm, has been a collaboration between Georgia Tech and Tempest Technologies. From the beginning of the project, UCLA and Tempest have collaborated closely on development of new adaptive optics methods based on adaptive filtering and control. MZA and ATK Mission Research have worked closely with UCLA, Georgia Tech, and Tempest to provide realistic simulations of the new methods for beam control and tracking. The most important evaluations of the new adaptive optics methods have been performed by MZA and ATK Mission Research. In these evaluations, MZA for the first time combined one of the new adaptive optics algorithms developed by UCLA with the Bayesian tracker developed by Georgia Tech and Tempest Technologies. That these new methods for HEL beam control and target tracking work together very well in such high-fidelity simulations is one of the greatest success stories of this MRI to date. In these simulations, the adaptive optics algorithm and Bayesian tracker worked simultaneously but independently. These evaluations by MZA suggest that planned future research to integrate the two methods should produce even greater performance enhancements.

The work under this project has included not only extensive theoretical and numerical research, but also substantial experimental research at Michigan Tech, UCLA, MZA, and the Air Force Institute of Technology (AFIT). UCLA has conducted experimental research on adaptive control of beam jitter. Also, Michigan Tech, MZA, ATK Mission Research and AFIT have conducted experimental research on the use of spatial light modulators to create wavefront errors equivalent to those produced by atmospheric turbulence. Expanded experimental research is a major part of the research planned for the next two and a half years under this MRI. The experimental research will serve two purposes: (1) reveal challenging problems inherent in the physics of beam control and sensing, thereby guiding our theoretical and numerical investigations and algorithm development; (2) demonstrate the practical utility of the methods developed in our research for beam control and tracking.

Chapter 2

Adaptive Control of Laser Beams

UCLA, TEMPEST TECHNOLOGIES,
MZA ASSOCIATES CORPORATION

Compared to the classical methods used in adaptive optics and beam steering and pointing, the methods developed at UCLA can improve the performance of directed-energy weapons such as the airborne laser (ABL) and the airborne tactical laser (ATL), as well as laser communications systems. High-fidelity wave-optics simulations of directed energy systems have shown significant performance improvements with the new adaptive control scheme [1]¹. Also, recent experiments in the Atmospheric Simulation and Adaptive-optics Laboratory Testbed (ASALT) at the Starfire Optical Range at the Air Force Research Laboratory, Kirtland AFB have demonstrated enhanced performance produced by UCLA's new adaptive control scheme for adaptive optics [2, 3].

UCLA's contributions to control of laser beams fall into two main categories: adaptive control and filtering for correction of higher-order wavefront errors adaptive optics [1, 2, 3, 4, 5], and adaptive control of tilt jitter [6, 7, 8, 9, 10, 11, 12, 13, 14, 15, 16, 17, 18, 19]. The two problem categories are closely related and are both present in adaptive optics systems. Adaptive control of higher-order wavefront errors usually involves control loops with many, often hundreds of channels corresponding to spatially distributed wavefront sensor measurements and deformable mirror actuators; adaptive control of tilt jitter involves two control channels and two or more sensor signals, but usually much higher temporal orders of the adaptive filter.

A brief discussion of adaptive optics in laser weapon systems should give some perspective to much of the proposed research. Adaptive optics (AO) refers to the use of deformable mirrors driven by active control loops that feedback wavefront sensor (WFS) measurements to compensate for turbulence-induced phase distortion of optical waves propagating through the atmosphere. These control loops reconstruct (i.e., estimate and predict) the phase profile, or wavefront, from the WFS data. The control loops in classical AO systems are linear and time-invariant (LTI), having fixed gains based on assumed statistics of atmospheric turbulence. Such control loops are not themselves adaptive in the sense in which the term *adaptive* is used in the control and filtering literature, where *adaptive* normally refers to updating control and/or filter gains in real time.

Adaptive compensation is needed in many AO applications because wind velocities and the strength of atmospheric turbulence can change rapidly, rendering any fixed-gain reconstruction algorithm far from optimal. UCLA research has introduced adaptive wavefront reconstruction algorithms that use recursive least-squares (RLS) lattice filters to predict the wavefront and estimate optimal reconstructor matrices that track unknown and time-varying turbulence statistics. In this

¹UCLA publications can be found at <http://www.beamcontrol.seas.ucla.edu>.

approach, an adaptive control loop augments a classical AO feedback loop. Results in [1, 20] have shown that UCLA’s adaptive control loops are robust with respect to modeling errors and sensor noise.

Figure 2.1 shows a schematic diagram for an adaptive optics problem in laser weapon system. This diagram represents roughly the high-fidelity ABL simulation in [1], as well as an array of laser weapons motivating the AFRL experimental testbed described in [2]. In such systems, actuators are distributed in a two-dimensional array over a deformable mirror. These actuators are driven to adjust the profile of the mirror surface and cancel the phase distortions induced in the high-energy laser beam as it propagates through atmospheric turbulence. A wave front sensor (WFS) measures the residual wavefront error, using an array of subapertures that sense the spatial derivatives, or slopes, of the phase profile on a grid interlaced with the locations of the actuators.

The purpose of AO system is to compensate the outgoing high energy laser for the wavefront error that will be induced by atmospheric turbulence, so that the laser forms a fixed, tight spot (image) on the target. The control system uses a beacon created by illuminating the target with a low energy laser as the basis for determining the commands to the deformable mirror required to cancel turbulence-induced phase distortion. Because the beacon is considered to be a distant point source, the wavefront propagating from the beacon would be very nearly a plane wave when it reached the mirror with no atmospheric turbulence. This plane wave is the desired set point for the control algorithm. If the wavefronts propagating from the beacon to the target travel through approximately the same atmosphere, then correcting the wavefront from the beacon should compensate for the turbulence effects on outgoing beam.

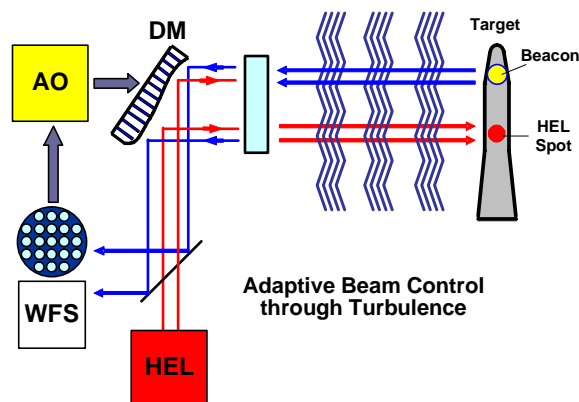


Figure 2.1: Diagram of a directed energy system with high energy laser (HEL). Key components of the beam control system: adaptive optics algorithm (AO), deformable mirror (DM), wavefront sensor (WFS).

2.1 Collaboration with AFRL and Industry on Adaptive Optics

2.1.1 Recent Results and Transitions in the Testbed at the Starfire Optical Range

An essential feature of UCLA’s research supported by AFOSR and HEL JTO has been close collaboration with the Air Force Research Laboratory (AFRL) and industry. UCLA and AFRL researchers have demonstrated a new adaptive control scheme for adaptive optics in experiments in the Atmo-

spheric Simulation and Adaptive-optics Laboratory Testbed (ASALT) at the Starfire Optical Range at the Air Force Research Laboratory, Directed Energy Directorate, Kirtland AFB. The adaptive control scheme was developed at UCLA in collaboration with researchers at the Air Force Research Laboratory. Initial results from this collaboration were presented in [2, 3].

Figure 2.2 shows a schematic diagram of the ASALT optical system. As shown in Figure 2.3, the adaptive control loop augments a classical AO loop to enhance beam control and imaging through turbulence. High-fidelity wave-optics simulations of directed energy systems have shown significant improvement in Strehl ratio (i.e., on-target intensity) and tracking jitter, and such enhanced performance now has been confirmed by the first experimental application of the new methods [2].

Experiments were performed in the ASALT laboratory to evaluate the performance of the quasi-adaptive version of the adaptive control loop. In the experiments, the first 150 modes from a set of frequency-weighted deformable-mirror modes were used by the adaptive control loop [2]. First, 3000 wavefront sensor frames were used to identify the adaptive filter gains, and then the performance of the adaptive controller was evaluated on 1000 frames independent of those used for identification.

For comparison, the same experiment was performed with only the classical AO and track loops, using the same 1000 frames for evaluation. For the turbulence scenario examined, the adaptive controller provided a nearly 50% increase in Strehl ratio and reduced the variability by more than 15%. Figure 2.4 shows example images from the evaluation sequences, further demonstrating the benefits of the adaptive controller.

2.1.2 Recent Transition to Aero-Optics

UCLA's methods for adaptive control in adaptive optics are being used in a Phase II SBIR to MZA Associates Corporation for mitigation of aero-optics effects in directed energy weapons, funded by MDA. This work is lead by Dr. Matthew Whitely and colleagues at MZA Associates Corporation, Albuquerque, NM, and Dayton, OH.

2.1.3 Future Collaboration

Currently, UCLA researchers are working with AFRL researchers, especially Dr. Darryl Sanchez and Lt. Robert Vincent, at the Starfire Optical Range (SOR), Kirtland AFB to implement the fully adaptive version of UCLA's latest adaptive optics algorithm in SOR's Atmospheric Simulation and Adaptive-optics Laboratory Testbed (ASALT). This collaboration should produce performance enhancements in the ASALT beam control system and should lead to several advances in adaptive optics. Two important areas of research will be the design of adaptive and optimal controllers to mitigate the effects of wavefront sensor noise in adaptive optics, and the development of system identification methods for obtaining high-fidelity models of complex adaptive optics systems. Both of these research topics will address critical problems that significantly limit performance in beam control systems at AFRL and in most defense and commercial applications. These problems can be studied to some extent with simulation models and university experiments; however, the more realistic testbed at AFRL's Starfire Optical Range enables much more relevant research, so UCLA plans to continue the collaboration represented by [2, 3].

UCLA plans to collaborate with Teledyne on control of their new liquid crystal spatial light modulator for wavefront control of high energy lasers. In recent months, Professors Gibson and Tsao have been invited to present our research to beam control groups at Northrop Grumman and Aerospace Corporation. Those visits initiated plans for future collaborations.

2.2 Recent Results and Transitions for Control of Liquid Crystal Beam Steering Devices

UCLA, AFRL and Teledyne Scientific Co. have collaborated to apply feedback and adaptive feedforward control to Teledyne's new liquid crystal beam steering devices [16, 15, 17]. These novel beam steering devices are being developed as actuators in jitter control and adaptive optics for applications to laser weapons and laser communications. Compared to standard mirrors used for beam control, the liquid crystal devices have the advantages of low power consumption and no moving parts.

Figure 2.5 and 2.6 show UCLA's beam control experiment with the prototype liquid crystal device. Figure 2.7 shows the block diagram of the overall control system including the liquid crystal device, the optical sensor, the disturbances and the control loops. An important question about the new devices is, can they deliver the control bandwidths comparable to those of fast steering mirrors? The experimental results in Figure 2.8 from [17] for a prototype device and more extensive experimental results in [16, 15, 17] are quite positive.

UCLA's adaptive control loop had to be modified to handle nonlinearities in the liquid crystal device resulting from a rate limit and quantization effects. Such nonlinearities have not been encountered in our research with fast steering mirrors [21, 13, 22, 14, 23, 24], but our newest adaptive control design accommodates the nonlinearities, resulting in no apparent performance degradation.

The close collaboration among UCLA, AFRL and Teledyne Scientific Co. has been very productive in several ways. First, the collaboration has illustrated the benefits of integrating considerations of control system performance into hardware design. Teledyne based the re-design of the driver for the two-axis device partly on the performance of an earlier single-axis device in control experiments at UCLA. The resulting two-axis device allowed the adaptive control loop to achieve much higher bandwidths than with the initial device. Second, UCLA students and faculty have had the opportunity of working with an exciting new class of hardware being developed in industry for Air Force missions. The experimental results reported in [16, 15, 17] were obtained from a jitter control experiment in UCLA's beam control laboratory with the Teledyne liquid crystal device. Most recently, UCLA Ph. D. student Pawel Orzechowski has worked with AFRL and Teledyne researchers to set up a similar experiment at the Starfire Optical Range, and we plan to continue this collaboration.

There are three nonlinearities in the liquid crystal device: a rate limit, an angle saturation and quantization. The effect of these nonlinearities is investigated in detail in [17], and a modification of the adaptive controller, based on a nonlinear model of the plant, is introduced to compensate partially for the nonlinearities. The analysis in [17] shows that the nonlinearities are significant for the jitter levels in Figure 2.8, but the original UCLA adaptive controller, which does not take the nonlinearities into account, handles the effects of the nonlinearities as well as the modified adaptive controller does. However, as illustrated by the output error for Axis 2 in Figure 2.9, when the jitter amplitudes are increased by only 33%, the adaptive controller based on a linear plant model fails, whereas the adaptive controller with the nonlinear modification performs very well. These results suggest one of the topics of the proposed research: modeling and identification of nonlinearities in liquid crystal beam control devices, and designing controllers that take the nonlinearities into account to optimize the performance of such devices.

Transition to Jitter Control in Relay Optics

During the following year, UCLA's adaptive jitter control methods will be used in a relay-optics experiment at AFRL under a Phase II SBIR to Tempest Technologies, funded by MDA. This work is lead by Dr. Ben G. Fitzpatrick of Tempest Technologies, Los Angeles, CA.

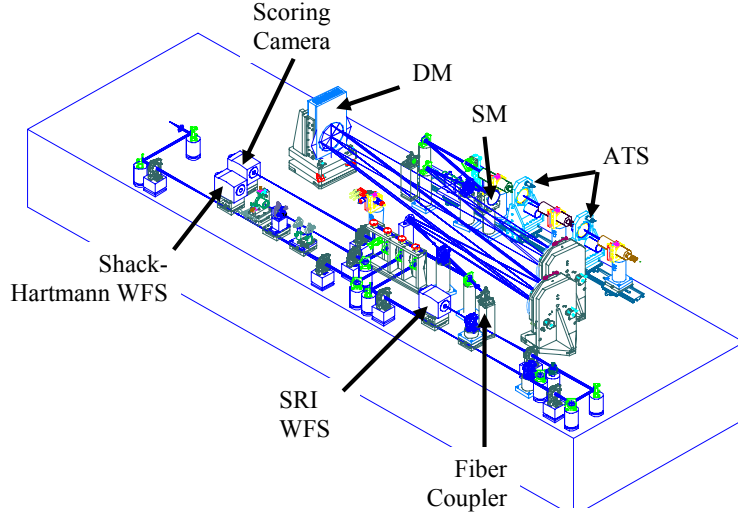


Figure 2.2: Atmospheric Simulation and Adaptive-optics Laboratory Testbed (ASALT) optical system, Starfire Optical Range, Kirtland AFB. The Self-Referencing Interferometer Wavefront Sensor (SRI WFS), an innovative sensor being developed at the Starfire Optical Range, was used for the experiments described.

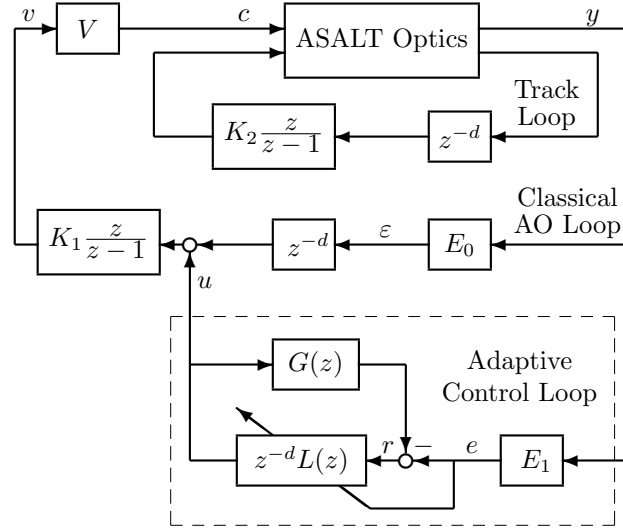


Figure 2.3: Block diagram of the digital control loops for adaptive optics. ASALT optics block represents the optical system in Figure 2.2.

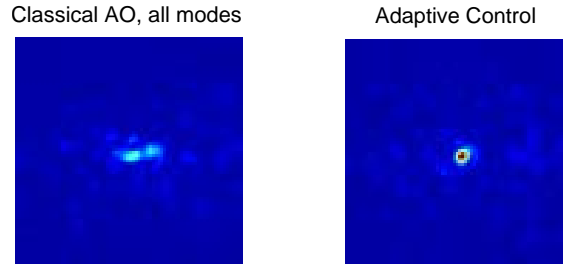


Figure 2.4: Representative closed-loop scoring camera images. Adaptive control produces tighter laser spot with greater intensity on target than classical adaptive optics (AO).

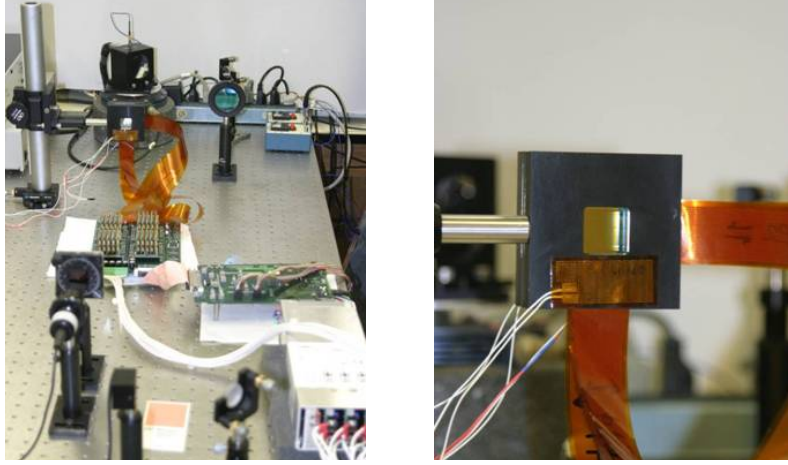


Figure 2.5: Left: UCLA beam control experiment with Teledyne's prototype liquid crystal beam steering device. Control sample and hold rate = 3125 Hz. Right: Close-up view of the liquid crystal device.

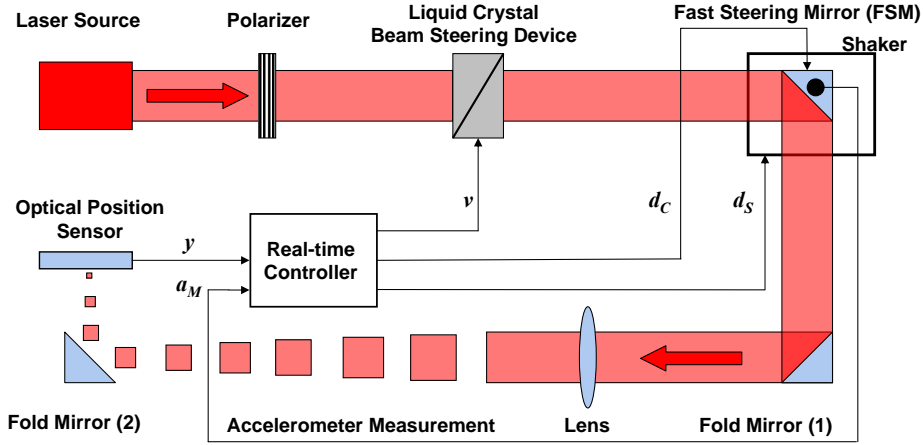


Figure 2.6: Diagram of UCLA beam control experiment with Teledyne's liquid crystal beam steering device.

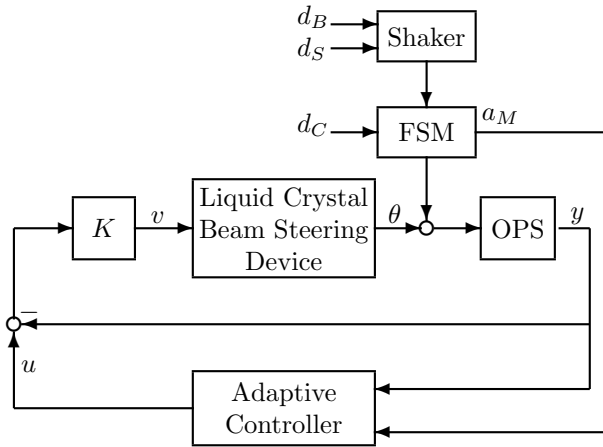


Figure 2.7: Block diagram of the control system. d_S = disturbance command to shaker; d_B = building vibration; d_C = disturbance command to FSM; d_M = response of FSM; θ = beam angle from liquid crystal beam steering device; y = beam position; OPS = optical position sensor; u and v = control commands.

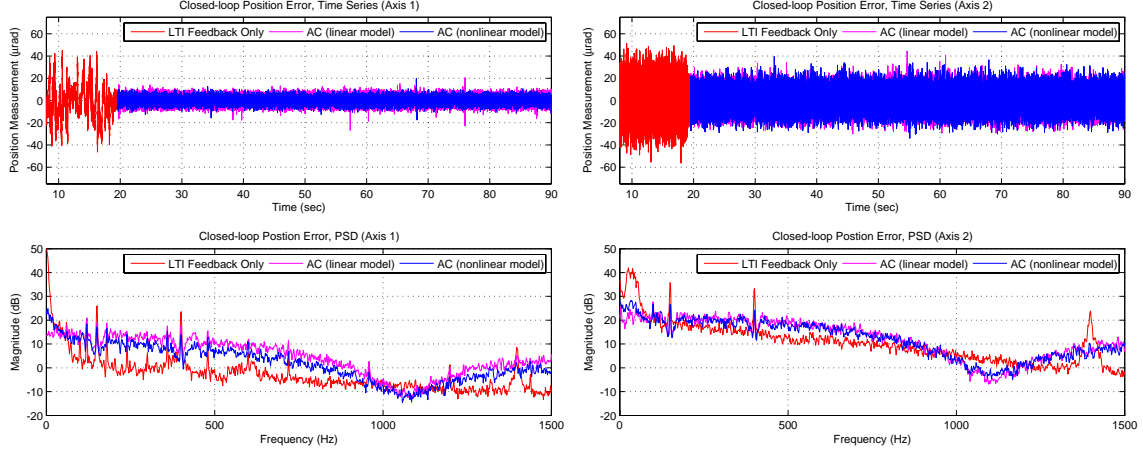


Figure 2.8: Disturbance rejection performance comparison for the horizontal axis (Axis 1) and the vertical axis (Axis 2). LTI feedback control (red); adaptive control (blue). Maximum lattice filter order $N = 10$. Jitter sources: building vibration, commands to fast steering mirror (FSM) and shaker.

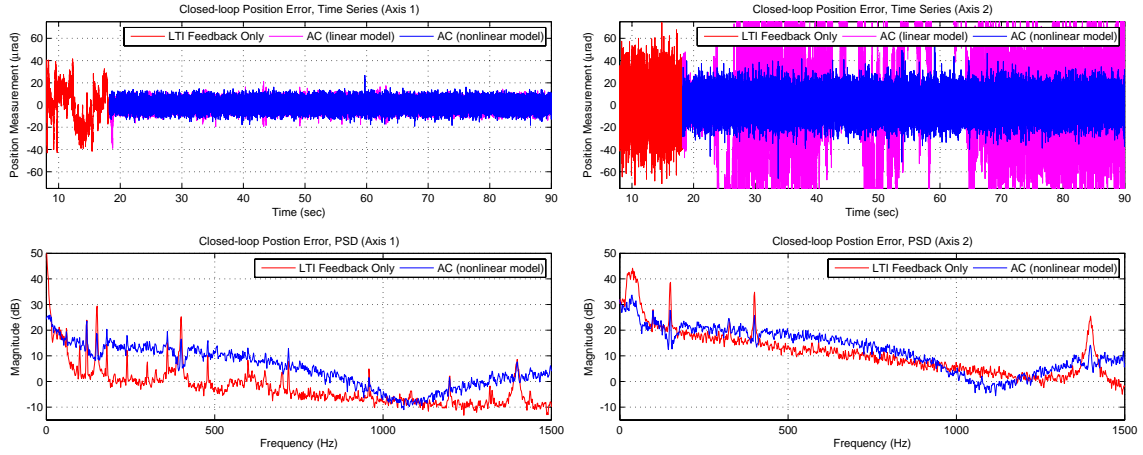


Figure 2.9: Performance comparison for jitter-command magnitudes increased by 33%: LTI feedback only, adaptive control loop with linear plant model \hat{G} and adaptive control loop with nonlinear plant model \hat{G}_{NL} . Output-error time series and corresponding power spectral densities (PSD) for steady-state responses are shown. Axis 1 (left) is horizontal, and Axis 2 (right) is vertical. Adaptive control begins at $t = 19$ sec.

Future Collaboration

UCLA faculty and students will continue the current collaboration with Dr. Dan Herrick and others at AFRL and Teledyne Scientific Co. on control of liquid crystal devices for beam steering. While the recent experimental research in UCLA's beam control laboratory on these devices has been quite productive, it is even more exciting now that UCLA's control algorithms are being implemented in the jitter control laboratory at AFRL's Starfire Optical Range at Kirtland AFB. Liquid crystal technology for beam control also is being developed by other defense contractors, including Raytheon, and we expect to develop collaborations with such companies.

Bibliography

- [1] Y.-T. Liu and J. S. Gibson, “Adaptive control in adaptive optics for directed-energy systems,” *Optical Engineering*, vol. 46, no. 4, April 2007.
- [2] T. A. Rhoadarmer, L. M. Klein, J. S. Gibson, N. Chen, and Y.-T. Liu, “Adaptive control and filtering for closed-loop adaptive-optical wavefront reconstruction,” in *SPIE Conference on Advanced Wavefront Control*, vol. 6306. San Diego, CA: SPIE, August 2006.
- [3] —, “Novel scheme for enhancing beam control in adaptive optics,” *SPIE Newsroom*, <http://spie.org/x8549.xml>.
- [4] Yu-Tai Liu and J. S. Gibson, “Adaptive optics with adaptive filtering and control,” in *American Control Conference*. Boston, MA: IEEE, June 2004.
- [5] Yu-Tai Liu, Neil Chen, and J. S. Gibson, “Adaptive filtering and control for wavefront reconstruction and jitter control in adaptive optics,” in *American Control Conference*. Portland, OR: IEEE, June 2005.
- [6] B.-S. Kim, S. Gibson, and T.-C. Tsao, “Adaptive control of a tilt mirror for laser beam steering,” in *Proc. of the American Control Conference*, Boston, MA, June 2004, pp. 3417–3421.
- [7] Néstor O. Pérez Arancibia, J. S. Gibson, and Tsu-Chin Tsao, “Adaptive control of MEMS mirrors for beam steering,” in *IMECE2004*. Anaheim, CA: ASME, November 2004.
- [8] Néstor O. Pérez Arancibia, Neil Chen, J. S. Gibson, and Tsu-Chin Tsao, “Adaptive control of a MEMS steering mirror for suppression of laser beam jitter,” in *American Control Conference*. Portland, OR: IEEE, June 2005.
- [9] —, “Adaptive control of a MEMS steering mirror for free-space laser communications,” in *Optics and Photonics 2005*. San Diego, CA: SPIE, August 2005.
- [10] N. O. Pérez Arancibia, N. Chen, S. Gibson, and T.-C. Tsao, “Adaptive control of jitter in laser beam pointing and tracking,” in *Proc. SPIE 6304, Free-Space Laser Communications VI*, San Diego, CA, Sep. 2006, 63041G.
- [11] —, “Variable-order adaptive control of a microelectromechanical steering mirror for suppression of laser beam jitter,” *Optical Engineering*, vol. 45, no. 10, pp. 104206–1–12, October 2006.
- [12] P. K. Orzechowski, J. S. Gibson, and Tsu-Chin Tsao, “Adaptive control of jitter in a laser beam pointing system,” in *American Control Conference*. Minneapolis, MN: IEEE, June 2006.
- [13] —, “Optimal jitter rejection in laser beam steering with variable-order adaptive control,” in *Conference on Decision and Control*. San Diego, CA: IEEE, December 2006.
- [14] —, “Optimal suppression of laser beam jitter by high-order RLS adaptive control,” *IEEE Transactions on Control Systems Technology*, vol. 16, no. 2, pp. 225–267.

- [15] P. K. Orzechowski, J. S. Gibson, Tsu-Chin Tsao, Dan Herrick, Milind Mahajan, and Bing Wen, "Adaptive rejection of optical jitter with a new liquid crystal beam steering device," in *Defense and Security Symposium*. Orlando, FL: SPIE, April 2007.
- [16] Dan Herrick, P. K. Orzechowski, J. S. Gibson, Tsu-Chin Tsao, Milind Mahajan, and Bing Wen, "An alternative beam alignment approach for tactical systems," in *Directed Energy Systems Symposium: Beam Control Conference*. Monterey, CA: DEPS, March 2007.
- [17] P. K. Orzechowski, "High-performance adaptive control of optical jitter in laser beam systems," Ph.D. dissertation, University of California, Los Angeles, Los Angeles, CA, 2007.
- [18] P. K. Orzechowski, J. S. Gibson, and T.-C. Tsao, "Characterization of Optimal FIR Gains and Minimum-variance Performance for Adaptive Disturbance Rejection," in *Proc. of the American Control Conference*, pp. 1908–1913, New York, NY, Jun. 2007.
- [19] N. O. Pérez Arancibia, *Adaptive Control of Opto-Electro-Mechanical Systems for Broadband Disturbance Rejection*. Los Angeles, CA: Ph.D. Dissertation, University of California, Los Angeles, 2007.
- [20] J. S. Gibson, C.-C. Chang, and B. L. Ellerbroek, "Adaptive optics: wavefront correction by use of adaptive filtering and control," *Applied Optics, Optical Technology and Biomedical Optics*, vol. 39, no. 16, pp. 2525–2538, June 2000.
- [21] P. K. Orzechowski, Tsu-Chin Tsao, and J. S. Gibson, "The effect of computational delay on performance of adaptive control systems," in *IMECE*. Chicago, IL: ASME, November 2006.
- [22] P. K. Orzechowski, J. S. Gibson, and Tsu-Chin Tsao, "Characterization of optimal FIR gains and minimum-variance performance for adaptive disturbance rejection," in *American Control Conference*. New York, NY: IEEE, July 2007.
- [23] N. O. Perez Arancibia, N. Chen, J. S. Gibson, and T.-C. Tsao, "Variable-order adaptive control of a mems steering mirror for suppression of laser beam jitter," *Optical Engineering*, vol. 45, no. 10, October 2006.
- [24] —, "Adaptive control of jitter in laser beam pointing and tracking," in *Proc. SPIE 6304, Free-Space Laser Communications VI*. San Diego, California: SPIE, September 2006.
- [25] R. R. Beland, "Propagation through atmospheric optical turbulence," in *IR/EO Handbook*, F. G. Smith, Ed. Bellingham, WA: SPIE Press, 1993, vol. 2, pp. 157–232.
- [26] J. W. Goodman, *Statistical Optics*. New York: John Wiley & Sons, 1985.
- [27] M. Belenkii and K. Hughes, "Beacon anisoplanatism," in *Proc. SPIE on Laser Systems Technology*, vol. 5087, 2003, pp. 69–82.
- [28] J. W. Goodman, *Introduction to Fourier Optics*. New York: McGraw-Hill Book Co., 1968.
- [29] R. A. Muller and A. Buffington, "Real-time correction of atmospheric turbulence degraded telescope images through image sharpening," *J. Opt. Soc. Am.*, vol. 64, pp. 1200–1210, 1974.
- [30] M. A. Vorontsov, G. W. Carhart, D. V. Pruidze, J. C. Ricklin, and D. G. Voelz, "Image quality criteria for an adaptive imaging system based on statistical analysis of the speckle field," *J. Opt. Soc. Am.*, vol. 13, pp. 1456–1466, 1996.

Chapter 3

HEL Propagation through Extended Tubulence

MICHIGAN TECH

Michigan Tech has conducted significant modeling efforts for laser beam propagation through horizontal paths on the order of 10 km to 20 km in length in support of our work in developing advanced, higher order, nonlinear beam control algorithms for deformable mirrors. This work has been aimed at understanding the “forward problem of beam control for high energy lasers in a tactical scenario. Tactical scenarios differ from ABL-like scenarios in that the propagation path is at lower altitudes due to the look-down, shoot-down aspect of tactical engagements. The consequence for optical propagation is stronger C_n^2 levels than at higher altitudes, and the possibility that thermal blooming effects will strongly impact the system performance. The isoplanatic angle is expected to be much smaller than the field of view of the target acquisition system in most tactical scenarios, and scintillation is expected to generally be strong. Additionally, there will not be a point-like beacon in the target plane for tracking and higher order wave front sensing purposes, and hence one must be created in an ABL-like manner, or the wave front information must be extracted from the scene. The hardware implications for tactical HEL systems include use of smaller apertures than ABL-type systems, and the use of lower energy, solid state lasers.

The physical model for a beacon creation system in a tactical HEL is shown in Fig. 3.1. An uncompensated outgoing laser, referred to as the beacon laser, is used to illuminate the target. Since there is no signal available suitable for wave front sensing, the beacon laser is, of necessity, uncompensated. As a result, the beam arriving at the target is affected by the turbulence present between the transmitter and the target. If the combination of path length and turbulence strength are sufficiently strong, the beam arriving at the target will be on average broader than the limit imposed by diffraction, will wander randomly, and will be speckled [25]. The surface of the target is modeled as being optically rough in the sense that the fine structure of the scattering surface causes the phase of the scattering surface to be uniformly distributed on $(-\pi, \pi)$ [26]. Additionally, the scattering surface is δ -correlated in space, and its rate of change is much faster than the integration time of wave front and imaging sensors. At the telescope pupil, this characteristic of the target surface will give rise to a phenomenon referred to as *laser speckle* [26]. Laser speckle effects include strong intensity and phase fluctuations arising from the random phase distribution of the scattering surface. Thus, the beacon field arises from a random intensity incoherent object which may be large relative to the diffraction limited spot, and additionally, at the wave front sensor receiver plane the incoming field will in general be corrupted with laser speckle effects. Some of the radiation scattered from the target will propagate back in the direction of the transmit/receive aperture, where it will

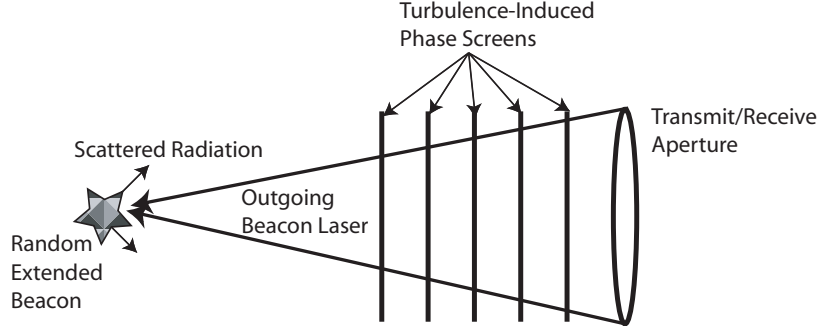


Figure 3.1: Physical model of the beacon creation process. A laser passes through the turbulent atmosphere and illuminates the target. Backscattered radiation passes back through the atmosphere to be used for wave front sensing.

be intercepted and used for wave front sensing.

The beacon field can be measured in various ways, and these measurements can be processed to estimate the phase of the impulse response for propagation through the atmosphere from the aim point on the target to the laser output aperture. This impulse response is denoted by $h_A(x_T, x_P, t)$, where x_T is a coordinate in the target plane, x_P is a coordinate in the laser output aperture plane, and t represents time. In general $h_A(x_T, x_P, t)$ is complex valued:

$$h_A(x_T, x_P, t) = |h_A(x_T, x_P, t)| \exp[j\phi_A(x_T, x_P, t)] \quad (3.1)$$

where $\phi_A(x_T, x_P, t)$ is the phase of the atmospheric propagation impulse response, and under anisoplanatic conditions $h_A(x_T, x_P, t)$ is a function of *both* beacon plane position and pupil plane position. In the context of adaptive optics control of the outgoing laser beam, the purpose of wave front sensing is to estimate $\phi_A(x_T, x_P, t)$ from the available measurements. It should be noted that the temporal behavior of turbulence and laser speckle effects are significantly different - in general we expect that the laser speckle effects evolve at a much higher rate than the turbulence effects, and this insight must be incorporated into any analysis of wave front sensing in this environment.

We now examine the characteristics of the beacon beam arriving at the target plane. We shall begin our analysis using results obtained from the Rytov theory of wave propagation through turbulence, which assumes weak field perturbations, though it must be noted that the assumption of weak perturbations is often violated in practice due to the combination of turbulence strength and path length. We shall use simulations later in this paper to obtain results for conditions where the weak fluctuation assumption is violated, with the result that the variance of the log-amplitude fluctuations saturates [25]. Consider a region of constant C_n^2 over a path of length L . The point statistics of the intensity fluctuations of the beacon beam arriving at the target can be derived from the variance of the log amplitude fluctuations σ_χ^2 . For a collimated beam propagating through this σ_χ^2 is given by [25]

$$\sigma_\chi^2 = 0.305k^{7/6}C_n^2L^{11/6}, \quad (3.2)$$

where the wave number is given by $k = 2\pi/\lambda$, where λ is the wavelength. The normalized variance of the intensity fluctuations at the target σ_I^2 are then given by

$$\sigma_I^2 = \frac{\langle (I - \langle I \rangle)^2 \rangle}{\langle I \rangle^2} = \exp(4\sigma_\chi^2) - 1, \quad (3.3)$$

where $\langle \cdot \rangle$ represents the statistical expectation operator. The transverse correlation length ρ_0 of a

collimated beam passing through this turbulent path is given by [25]

$$\rho_0 = (1.46k^2C_n^2L)^{-3/5}. \quad (3.4)$$

The mean square short-term beam radius due to turbulence $\langle \rho_S^2 \rangle$ is [25]

$$\langle \rho_S^2 \rangle = \frac{4L^2}{(kD)^2} + \left(\frac{D}{2}\right)^2 + \frac{4L^2}{(k\rho_0)^2} \left[1 - 0.62 \left(\frac{\rho_0}{D}\right)^{1/3}\right]^{6/5}, \quad (3.5)$$

and we note that this expression describes the mean square instantaneous spot radius in the target plane. The intensity pattern of the beacon laser at the target will also wander due to turbulence-induced tilt, leading to a generally much larger long-term mean square spot radius. Since we are primarily interested in making high speed measurements, evaluating Eq. (3.5) is sufficient for our purposes. The isoplanatic angle θ_0 for this path is given by [25]

$$\theta_0 = \left(1.09k^2C_n^2L^{8/3}\right)^{-3/5}, \quad (3.6)$$

and the isoplanatic angle projected into the target has dimension $\theta_0 L$.

We now evaluate σ_χ^2 and both ρ_S and $\frac{1}{2}\theta_0 L$, the radius of a spot in the target plane subtending θ_0 , for the case of a fixed tactical engagement-like scenario, with path length $L = 20$ km, $\lambda = 1$ μ m, transmitter diameter of $D = 1$ m, and $10^{-17} \leq C_n^2 \leq 10^{-15} \text{ m}^{-2/3}$. We have two purposes for these calculations: (1) to discover the approximate value of C_n^2 for which σ_χ^2 reaches the saturation regime of $\sigma_\chi^2 \geq 0.3$ for this optical path; and (2) to compare the short term spot radius to the radius of a θ_0 -sized spot in the target plane. The results are presented in Fig. 3.2. Figure 3.2(a) presents the results for σ_χ^2 vs. C_n^2 , and Fig. 3.2(b) presents the results for ρ_S and $\frac{1}{2}\theta_0 L$ at the target plane vs. C_n^2 . Inspection of Fig. 3.2(a) shows that for the atmospheric path modeled, turbulence characterized by $C_n^2 < 2 \times 10^{-16}$ yields values of σ_χ^2 which are below the saturation regime. At altitudes below 2 km C_n^2 values in the range $10^{-17} \leq C_n^2 \leq 10^{-15} \text{ m}^{-2/3}$ are common, and we conclude that many scenarios of practical interest for low altitude beam projection systems will result in the need to operate in the presence of saturated σ_χ^2 conditions [25]. Higher altitude systems will also experience a similar operational situation, though longer optical paths are permitted before saturated σ_χ^2 conditions arise.

Inspection of Fig. 3.2(b) shows that the Rytov theory predicts that the spot radius due to short term beam spreading is in the range of 1.8 to more than 20 times the radius of an isoplanatic angle-sized patch in the target plane, $\frac{1}{2}\theta_0 L$. If we assume the target is on the order of the same size as ρ_S plus the beam wander, or bigger, then most or all of the light arriving at the target plane will be scattered. If the target is optically rough, some light from each illuminated point on the target plane will be scattered back in the direction of the aperture. Because $\rho_S \gg \frac{1}{2}\theta_0 L$, light arriving at the aperture from different points on the target will have travelled through significantly different atmospheric paths. Light corrupted with the aberrations obtained from these many optical paths arrives superimposed at the aperture, where it is used in the wave front sensing system. Because the light arrives superimposed from so many directions which are in general separated by more than θ_0 , conventional wave front sensing processes will not estimate the same turbulence-induced wave front error that would be computed if a point source beacon were present. In most cases of practical interest, the errors between the wave front estimated from the extended beacon, and the wave front which would have been estimated if a point source beacon were present are significant, and severely degrade the ability of the beam control system to focus light on a small spot in the target plane [27]. This is the essence of the effect referred to as beacon anisoplanatism. This topic is addressed in more detail in the paper *Fundamental considerations for wave front sensing with extended random beacons*, by Roggemann, which was presented at the SPIE meeting in Denver, in August, 2004. This paper is included in the appendix.

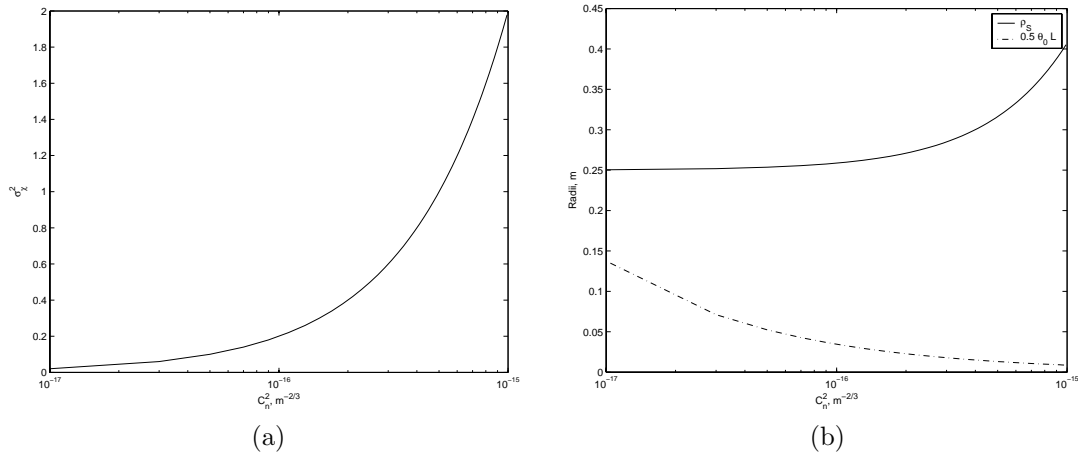


Figure 3.2: (a) σ_χ^2 at the target plane vs. C_n^2 for $L = 20$ km, and $\lambda = 1 \mu\text{m}$. (b) ρ_S and $\frac{1}{2}\theta_0 L$ at the target plane vs. C_n^2 for the same optical path, with transmitting aperture diameter $D = 1$ m.

The key findings of the modeling work described above are that the total implications of the lack of a cooperative beacon in tactical HEL scenarios is likely the most fundamental performance limitation. Both tracking and higher order compensation are affected by this issue. As we will show later, when an appropriate tracking signal is present, advanced, non-linear deformable mirror control algorithms are very effective in providing a high Strehl ratio at the target. Likely, technological solutions to these problems for HEL beam control will have the following key elements:

1. Tracking information obtained from some element of the target or scene. Work along the lines of the extended target tracking efforts underway at Georgia Tech offers hope in this area, but the algorithms will have to be extended to work in a cluttered background environment.
2. A beacon laser will still be required to provide higher order wave front sensing information, and processing the resulting measurements into useful deformable mirror commands will require non-linear algorithms.
3. Extremely high speed computing will be required for these approaches to be successful.

We now move on to a top level discussion of the extensive simulation efforts underway at Michigan Tech.

Simulation of a tactical HEL path requires a multi-layer model of the turbulence to capture the scintillation and anisoplanatic aspects of the turbulence effects. Since the optical path we have modeled so far has constant C_n^2 we model the turbulence with 10 equal strength, but statistically independent phase screens. These screens are generated with a von Karman power spectral density using a well-established technique based on spatial filtering of a white noise process. The first screen is placed in the aperture of the transmit/receive telescope, and the last is placed a finite distance in front of the target. Each screen is treated as a phase object, so that passage through the screen causes the phase of the optical wave to change, but not its amplitude. A wave optics propagator based on the angular spectrum propagator [28] is used to model all of the propagations between screens, and between the last screen to the target. This approach has been widely used in many propagation studies, and is the one implemented in widely used programs such as WaveTrain. We chose the approach because it was very straight forward to extend the vast library of existing code we had developed and validated under other programs, and because it offered maximum flexibility

in developing the non-linear algorithms for deformable mirror control. Typical results of simulations of this sort are shown elsewhere in this report, and our results are very similar to these.

Chapter 4

Novel Methods for Wavefront Sensing and Beam Control

MICHIGAN TECH

4.1 Optimal Beam Control

We consider beam propagation scenarios for which a pupil-plane field $f(u)$ over an aperture region $u \in \mathcal{A}$ is transmitted through a propagation medium that is characterized by an inhomogeneous and random medium with an associated Green's function $h(x, u)$, where u is a two-dimensional spatial index in the pupil plane and x is a two-dimensional spatial index in the target plane. The target-plane field, then is

$$g(x) = \int_{\mathcal{A}} h(x, u) f(u) du,$$

which is, in general, a random quantity because of the randomness in the propagation kernel h . The objective of wavefront sensing and beam control is to generate a transmitted beam that maximizes in some sense the localized energy $|g(x)|^2$ at the target. One common method for quantifying the localized energy of a transmitted beam is:

$$I_r = \int_{|x| \leq r} |g(x)|^2 dx,$$

so that I_r quantifies the total intensity over a disc of radius r . Because the propagation kernel is random, the localized intensity I_r is, in general, a random quantity.

4.2 Time-averaged optimal beam control

One approach to dealing with the randomness of the propagation kernel is to optimize first- or second-order moments of the localized intensity I_r . We have shown that when one chooses to optimize the expected intensity $E[I_r]$, then the optimal beam is the principle eigenfunction (the largest eigenvalue's eigenfunction) for the following kernel:

$$H(u, u') = \int_{|x| \leq r} E[h^*(x, u) h(x, u')] dx.$$

Initial studies have shown that, for random media such as short-path or extended-path turbulence, a beam specified in this manner provides little, if any, performance enhancement over an uncompensated beam. Because of this, beam control must be accomplished for each individual realization of the random Green's function.

4.3 Optimal beam control when the propagation kernel is known

Optimization of the localized energy of a transmitted beam through a medium that is characterized by the Green's function $h(x, u)$ requires that the transmitted beam be determined as the principle eigenfunction for the following kernel;

$$\mathcal{H}(u, u') = \int_{|x| \leq r} h^*(x, u) h(x, u') dx.$$

We have also shown that this eigenfunction can be efficiently computed using an iterative transform algorithm, and this method provides guaranteed convergence to the optimal beam. However, the Green's function is rarely known, so some method of adaptive inference must be utilized in most situations.

4.4 Field Models for Noncooperative Targets

Wavefront sensing and beam control in the presence of a noncooperative target typically requires that the target itself be illuminated to form a reference field for sensing and control. The field that presents itself at the sensor's pupil, then, can be used to estimate the wavefront and make inferences about the propagation medium. However, because the reference field that reflects from the target has extended spatial extent, the field at the sensor pupil does not allow for direct inference about the medium.

We refer to the complex amplitude of the field that is reflected from the target as $g_t(x)$, and this field is related to the field that appears in the pupil as:

$$f_p(u) = \int h^*(x, u) g_t(x) dx,$$

where we have assumed that reciprocity holds for the the medium's propagation kernel. That is, the kernel for propagation from the pupil to the target is $h(x, u)$, and the kernel from propagation from the target to pupil is $h^*(x, u)$. Whereas we assume that the medium is, in general, inhomogeneous and its Green's function is unknown, we do assume that the Green's function does not change during a particular observation interval. The mutual intensity for the pupil-plane field over an observation interval is:

$$J_p(u, u') = \langle f_p(u) f_p^*(u') \rangle,$$

where $\langle \cdot \rangle$ denotes a time average over the observation interval. Accordingly,

$$\begin{aligned} J_p(u, u') &= \langle f(u) f^*(u') \rangle \\ &= \int \int h^*(x, u) \langle g_t(x) g_t^*(x') \rangle h(x', u') dx dx' \\ &= \int \int h^*(x, u) J_t(x, x') h(x', u') dx dx', \end{aligned}$$

where $J_t(x, x')$ is the mutual intensity for the field reflected from the target.

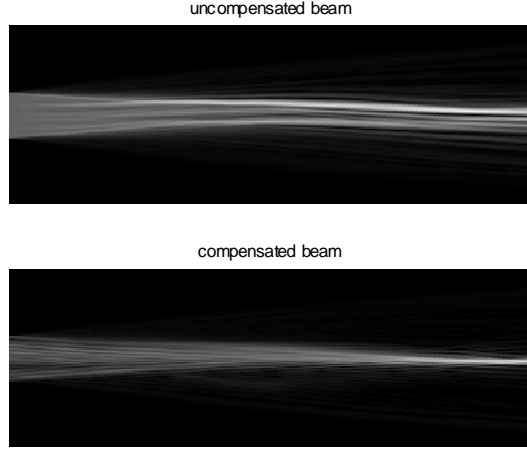


Figure 4.1: An example illustrating pupil-plane adaptive compensation with a noncooperative target. Both the uncompensated and compensated beam profiles are shown.

If the observation time interval is long compared with the coherent *speckle* variations of the reflected field, then the target-plane mutual intensity will be well approximated by:

$$J_t(x, x') \simeq b(x)\delta(x, x'),$$

where $b(x)$ is the average intensity that is reflected at the target, sometimes called the 'beacon'. Accordingly, the mutual intensity in the pupil plane is

$$J_p(u, u') \simeq \int h^*(x, u)h(x, u')b(x)dx.$$

4.5 Pupil-plane Wavefront Estimation and Beam Control

The principle eigenfunction for the pupil-plane mutual intensity, when used to propagate a beam to the target, will have the property that

$$I_b = \int b(x)|g(x)|^2 dx$$

is maximized. Because of this, this eigenfunction can be used in an adaptive optics system for 'optimal' beam control. The measurement and processing steps are outlined below:

1. Utilize a shearing interferometer or similar instrument to measure the pupil-plane mutual intensity;
2. Determine the principle eigenfunction for the pupil-plane mutual intensity; and
3. Utilize the principle eigenfunction as the transmitted beam.

An example of the utilization of this method is shown in Figure 4.1. The beacon intensity, along with the uncompensated and compensated beams are shown in Figure 4.2.

The difficulty with this method is that the pupil-plane mutual intensity is a four-dimensional function, and its measurement can be challenging. In the next section we discuss a method whereby image-plane measurements are used to estimate and correct the field.

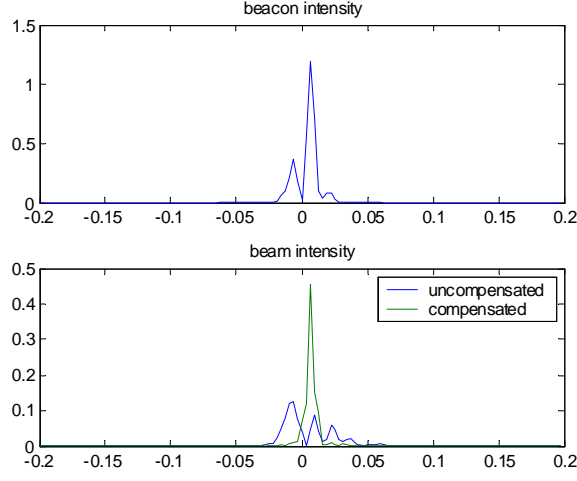


Figure 4.2: The beacon intensity and beam intensities for the pupil-plane adaptive compensation example with a noncooperative target.

4.6 Image-plane Wavefront Estimation

Suppose an adaptive field-compensator is placed in the system's pupil, and an image-plane intensity is recorded in the focus plane for the system's optics. This image intensity will be related to the pupil-plane field as:

$$i(y) = \left| \int f_p(u) \psi(u) e^{-j \frac{2\pi}{\lambda d_i} u \cdot y} du \right|^2,$$

where $\psi(u) = a(u)e^{j\phi(u)}$ is the pupil-plane field compensation. If the compensation is selected to maximize the *image sharpness* defined as:

$$\mathcal{S} = \int s(y) i(y) dy,$$

where $s(y)$ is a non-negative sharpness window, then the optimal compensation will be the principle eigenfunction for the following kernel:

$$\mathcal{H}_s(u, u') = \int h^*(x, u) h(x, u') b(x) dx S \left(\frac{u' - u}{\lambda d_i} \right),$$

where S is the Fourier transform for the sharpness window. An example of the utilization of this method with a Gaussian sharpness window with a full-width at half maximum (FWHM) equal to $\lambda d_i / D$ is shown in Figure 4.3. The beacon intensity, along with the uncompensated and compensated beams are shown in Figure 4.4.

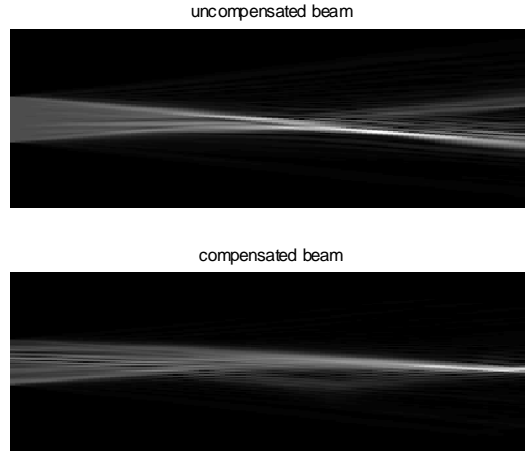


Figure 4.3: An example illustrating image-plane adaptive compensation with a noncooperative target. Both the uncompensated and compensated beam profiles are shown.

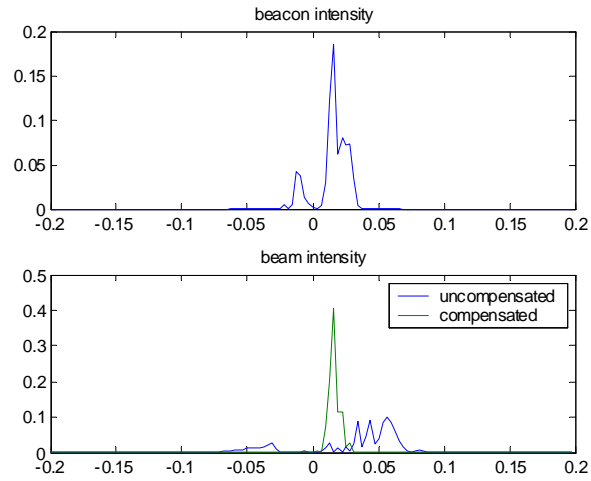


Figure 4.4: The beacon intensity and beam intensities for the image-plane adaptive compensation example with a noncooperative target.

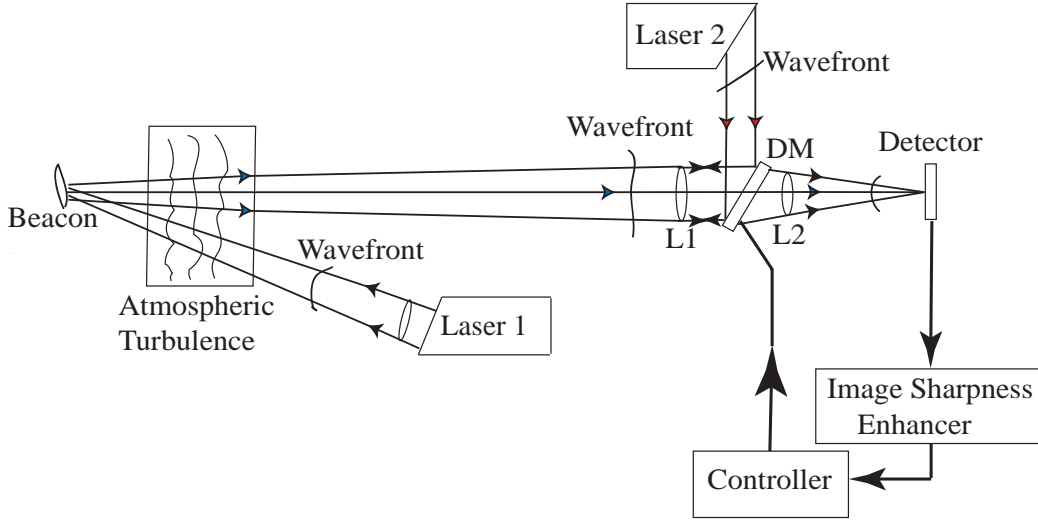


Figure 4.5: Deformable mirror control based on optimizing an image sharpness metric.

4.7 Non-linear Higher Order Deformable Mirror Control

Significant performance limitations arise for wave front sensing and deformable mirror control in the tactical HEL environment from beacon anisoplanatism, strong scintillation, and the lack of a cooperative tracking beacon. Phase difference measuring devices, such the Hartmann sensor, are subject to large errors from these issues. Having experimented extensively with phase difference measuring devices in the tactical HEL scenario, we decided to pursue a deformable mirror control scheme which does not strictly work in phase space, but rather, seeks to maximize some intensity-based measure of performance by controlling the phase falling on the pupil with a deformable mirror. Our work is an extension of an idea which has its basis in the image sharpness metric work of Muller and Buffington [29], and has been recently, and successfully extended by Vorontsov [30]. Deformable mirror control algorithms based on these image quality measures are inherently non-linear, since there is no linear relationship between the phase correction and the intensity measurement. We have shown under this project that deformable mirror control based on this concept can provide a significant performance improvement over conventional Hartmann sensor-base wave front control, but at the cost of requiring significant real-time processing capability. Excellent tracking of the target to remove turbulence-induced tilt errors must be provided in either case.

The block diagram for the system we are studying is shown in Fig. 4.5. An uncompensated beacon laser is used to illuminate the target. Light scattered from the target is received by the aperture, and an image is formed. The deformable mirror control algorithm seeks a set of deformable mirror commands which optimize an image sharpness metric in the image plane. When the optimal deformable mirror figure is found, the HEL is fired. In simulation the HEL beam is propagated to the target, and various measures of performance are computed. It must be noted that this approach requires tilt control information be obtained from some source other than the beacon laser, since due to reciprocity, the return beam has no tilt information. For our purposes, we presume that a tilt-only beacon is present in the scene, and only use the light emanating from this source to obtain tilt correction information. In an actual application information from the scene itself would likely be used to get tilt correction information.

The basic idea of this deformable mirror concept is to treat the operation of finding the optimal deformable mirror commands as an optimization problem. Let the deformable mirror command

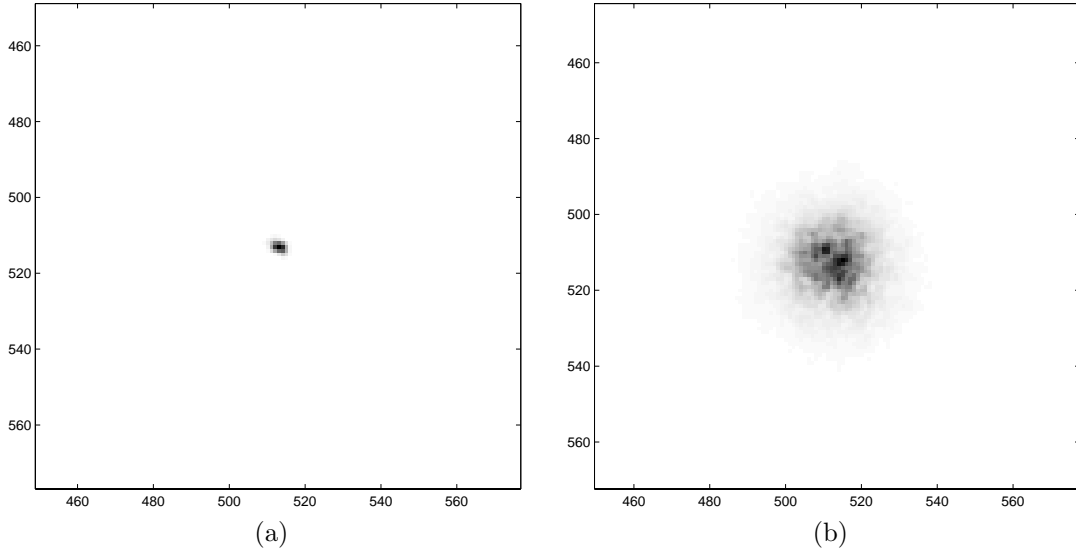


Figure 4.6: (a) Target intensity due optimizing the integrated square intensity $J_1(\alpha)$; (b) associated target intensity which would arise with only tilt correction. In both cases

vector be represented by α . In the paradigm describe above, the measured image of the scattered beacon laser is a function of α which we refer to as $I(x_i, \alpha)$, where x_i is an image plane coordinate. Our presumption, which has been born out by simulation experiments, is that the α which optimizes a measure of the quality of $I(x_i, \alpha)$ is an appropriate correction to apply to the outgoing beam. We iterate on the vector α to optimize an objective function we will generically refer to $J_m(\alpha)$, where the subscript m refers to an index on a specific image quality metric. As an example, consider use of the $J_1(\alpha)$ metric proposed by Muller and Buffington given by

$$J_1(\alpha) = \int I^2(x_i, \alpha) dx_i \quad (4.1)$$

Figure 4.6 shows the result of one optimization of $J_1(\alpha)$ for a tactical HEL scenario with $C_n^2 = 9.56 \times 10^{-16} \text{m}^{-2/3}$, with tilt correction present. Figure 4.6(a) shows the result for propagation through a single realization of an extended atmosphere in tactical HEL-like conditions using adaptive optics compensation; Fig. 4.6(b) shows the results for the case where only tilt correction was present. Comparison of these two results shows clearly that deformable mirror control based on non-linear optimization of image sharpness metric holds significant promise.

While some success has been achieved using the $J_1(\alpha)$ metric, we have obtained better performance with metric

$$J_3(\alpha) = \int I(x_i, \alpha) M(x_i) dx_i, \quad (4.2)$$

where $M(x_i)$ is a mask in the image plane. Essentially, the $J_3(\alpha)$ metric seeks to find a deformable mirror command vector α which maximizes the energy falling inside some region in the image detector plane. We have had excellent results with this approach, and an example is presented in Fig. 4.7. Figure 4.7 shows the average encircled energy in the target plane for the tactical HEL scenario with $C_n^2 = 19.12 \times 10^{-16} \text{m}^{-2/3}$. The three curves shown are encircled energy for the cases of no compensation (the NOCOMP curve), tilt correction using a cooperative beacon plus higher order correction based on least squares reconstruction from Hartmann wave front sensor outputs (the HWFS curve), and for tilt correction using a cooperative beacon plus higher order correction

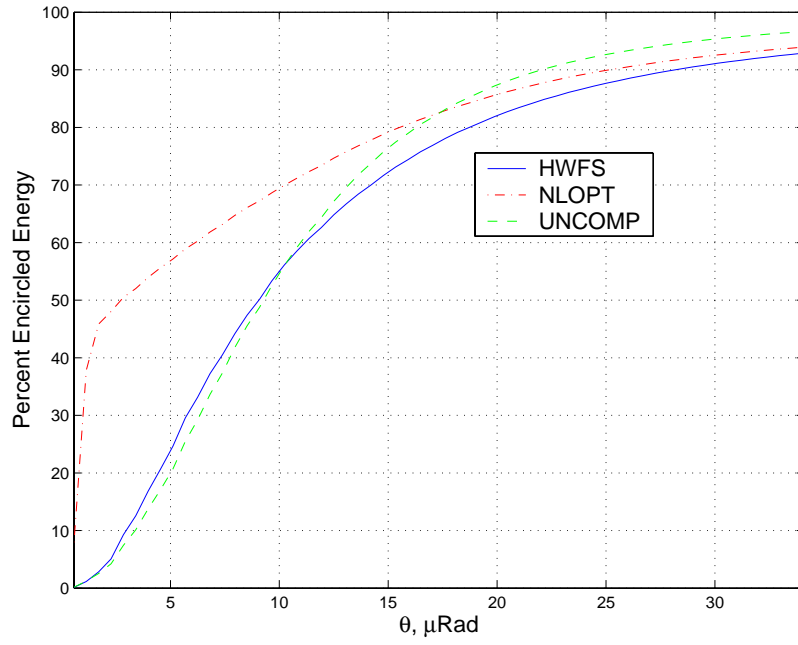


Figure 4.7: Percentage encircled energy in the target plane for $C_n^2 = 19.12 \times 10^{-16} \text{m}^{-2/3}$.

obtained from optimizing the J_3 metric (the NLOPT curve). Inspection of Fig. 4.7 The promise of the non-linear approach to controlling the deformable mirror is clear. The complete set of results obtained so far are included in the Kizito dissertation provided as an addendum to this report.

Chapter 5

Modeling and Simulation of HEL Wavefront Propagation

MZA ASSOCIATES CORPORATION

5.1 Introduction

Since April of 2006, MZA Associates Corporation (MZA) has been supporting the University of California at Los Angeles (UCLA) as a subcontractor on a grant from the Air Force Office of Scientific Research (AFOSR) sponsored by the High Energy Laser Joint Technology Office (HEL-JTO). This report summarizes the work accomplished over the period from 1 April 2006 through 31 October 2007. MZA supported this effort in the following areas:

- Phase screen generation for numerical simulation of long time series laser beam propagation through atmospheric turbulence.
- Closed loop tracking performance as a function of the spatial frequency content of atmospheric turbulence screens.
- **MATLAB**® version of the North American Aerospace Defense Command (NORAD) SGP4/SDP4 orbital propagator and study on energy transfer to orbital assets.
- Implementation of the Extreme and Percentile Environmental Reference Tables (ExPERT) atmospheric data into the Scaling for HEL and Relay Engagements (SHaRE) **MATLAB**® toolbox.
- Implementation of an adaptive controller (developed by UCLA) in **MATLAB**®/Simulink® and WaveTrain™.
- Laboratory simulation of atmospheric turbulence and aero-optic disturbances using spatial light modulators.

5.2 Accomplishments

Over the 19 months of this effort, MZA has accomplished a significant amount of research on high energy laser (HEL) propagation through the atmosphere. The majority of the work was related to the generation and implementation in WaveTrain™ of phase screens for long-time series closed-loop wave optics simulations. Much of this work was an extension of the work completed under this effort

by Mission Research Corporation and, subsequently, Alliant Techsystems (ATK). A brief summary of the each of the accomplishments listed above will be given in this section.

5.2.1 Phase Screens for Long Time Series Wave Optics Simulations

In this section we describe the progress made towards implementation of new atmospheric phase screens in *WaveTrain*TM which has been made by integrating the products of a series of separate efforts within MZA. The overall effort has been subsidized by several funding sources including internal MZA funding, Small Business Innovative Research (SBIR) funding, the Airborne Laser (ABL) program, as well as this contract. The overall effort has amounted to developing new atmospheric modeling classes within the *WaveTrain*TM code. The following subsections summarize the basic improvements which have been implemented as a result of this effort

Atmospheric Modeling Classes

When the atmospheric model for *WaveTrain*TM was originally developed in 1996, it was implemented in a manner so as to achieve certain efficiencies which, although appropriate for computational resources at the time, have now become irrelevant due to increased processor speed and memory. As a result, the code was not as modular and was made more complex than it now needs to be. One goal of this effort is to simplify and generalize the interface to the atmospheric model to make it more expandable and flexible so that new capabilities can be easily added using MZA's *tempus*TM plug-and-play methodology.

The new atmospheric model is implemented as a series of new C++ classes integrated into *WaveTrain*TM. Descriptions of the major new *WaveTrain*TM classes are provided in Table 5.1. The *wtPhaseScreen* class, and those derived from it, are documented with inline comments in the *WaveTrain*TM source code repository. The *PhaseScreen* and *Atmosphere* classes are also documented inline and provide standard *WaveTrain*TM system documentation in the *WaveTrain*TM System library.

Table 5.1: Descriptions of the major new atmospheric *WaveTrain*TM classes

Class Name	Description
<i>wtPhaseScreen</i>	The base class for the implementation of different phase screen computational and representational models. All new phase screen implementations derive from this base class to allow the wrapper code contained in the following two classes to manipulate different phase screen implementations with the same logic
<i>PhaseScreen</i>	<i>tempus</i> TM System which implements a phase screen logic
<i>Atmosphere</i>	Composite <i>tempus</i> TM system which wraps logic around a sequence of <i>PhaseScreen</i> objects in order to implement the complete atmosphere

New Method for computing Phase Screens

The original phase screens implemented in *WaveTrain*TM, based on a Fourier spectrum method, can be made to approximate correct low spatial frequency statistics at a sometimes significant computational

cost. MZA has implemented two new methods for generating phase screens which are approximately correct at low spatial frequencies.

A major drawback of the Fourier spectrum method of generating phase screens is that it requires the phase screen to be generated over a finite region predefined at the time the screen is generated. This results in having to store in memory the entire phase screen all at once even when only a small segment is needed and is very inefficient in the cases when the low frequency statistics of the screen are important. The two new phase screen generation methods are potentially infinitely extensible in order to allow slewing through very large areas of the phase screen without having to have held the entire screen in memory all at once. Furthermore, this capability provides the possibility that disconnected segments of the same correlated screen can be generated to handle multi-static propagation cases.

Previously, Dr. Eric Magee developed, under this effort and while at Mission Research Corporation and ATK, a technique for generating infinitely extensible phase screens having approximately correct low spatial frequency statistics using a Fourier series (FS) approach. In this method, a series of random Fourier coefficients are generated whose sum when evaluated at a given point within the phase screen results in an optical path difference (OPD) having the correct magnitude and relationship to neighboring points to represent an arbitrarily specified power spectral density (PSD) or structure function. For atmospheric phase screens the PSD used is typically Kolmogorov, however, the same routine has been used to generate Gaussian-correlated phase screens having similar characteristics to aero-optical effects. This capability was recoded in C++ and was added to WaveTrain™ as the class `FSScreen` which is derived from the base class `wtPhaseScreen`.

The technique is based on the decomposition of the random phase into a modified FS expansion,

$$\phi(x, y) = \sum_{n=-N/2}^{N/2} \sum_{m=-N/2}^{N/2} c_{n,m} \exp[j2\pi(f_{x_n}x + f_{y_m}y)] \quad (5.1)$$

where the $c_{n,m}$ are the random complex coefficients, and f_{x_n} and f_{y_m} are the user defined x - and y -spatial frequencies. The Frequencies are not constrained to harmonics as in the discrete Fourier transform (DFT). We use logarithmically spaced frequencies

$$f_n = \alpha f_{n-1} \quad (5.2)$$

$$\alpha = \left(\frac{f_{\max}}{f_{\min}} \right)^{1/(N-1)} \quad (5.3)$$

$$\Delta f_n = 2f_{\min} \alpha^n \frac{\alpha - 1}{\alpha + 1} \quad (5.4)$$

$$\Delta f_0 = 2f_{\min} \left(1 - \frac{\alpha - 1}{\alpha + 1} \right) \quad (5.5)$$

where the f_n are the spatial frequencies, α is the logarithmic growth parameter, and N is the number of frequencies between the minimum spatial frequency, f_{\min} , and the maximum spatial frequency, f_{\max} . The statistics of the $c_{n,m}$ are circular complex Gaussian with variance determined by the desired PSD of the phase screen

$$E \left\{ |c_{n,m}|^2 \right\} = \Delta f_{x_n} \Delta f_{y_m} \Phi_k(f_{x_n}, f_{y_m}) \quad (5.6)$$

where where $\Phi_k(f_x, f_y)$ is the PSD of the phase variations. The main advantage of the FS phase screen is that once the coefficients and spatial frequencies are determined, the phase screen is defined for all points in a plane. An example phase screen at various resolutions is shown in Fig. 5.1(a)-(c). The sample phase structure function is shown in Fig. 5.1(d). This plot also shows the theoretical structure function (in black) and the expectation of the structure function given the spatial frequency content of the phase screen.

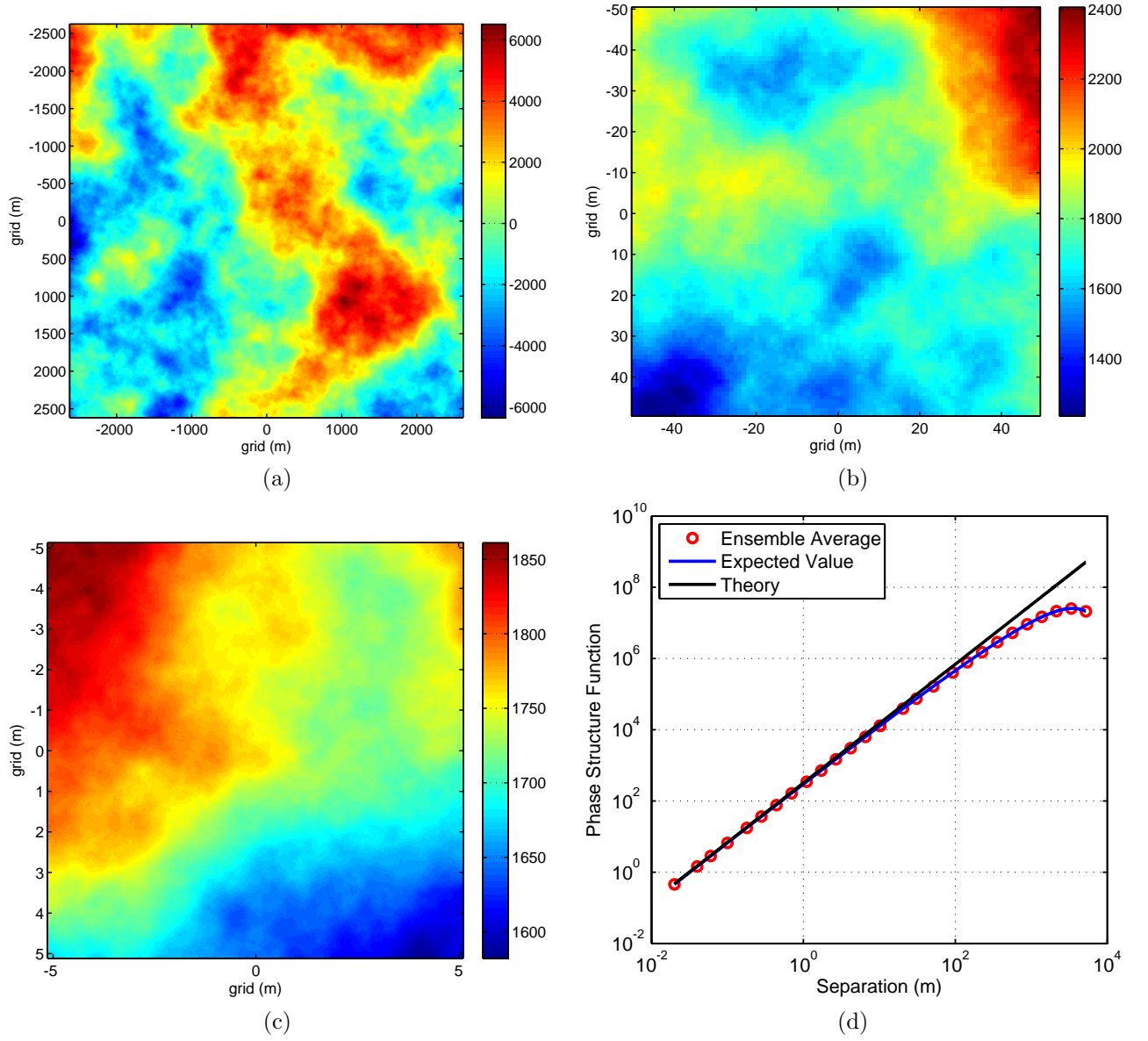


Figure 5.1: Example phase screens [(a)-(c)] generated using a modified FS with a minimum spatial frequency of 0.0001 m^{-1} . The structure function for an ensemble of 5000 independent screens is shown in (d).

Under a separate effort, Dr. Russ Butts developed a technique for correct and extensible phase screens based on the conditional probability density functions (CPDF). The original implementation was in **MATLAB**®. Dr. Richard St. John developed a Java-based tool for constructing the screens in a manner consistent with the wave-optics codes. As shown in Fig. 5.2, we currently have a Java GUI that can define a sparse grid with a given total physical extent. The grid for the screen can be iteratively refined and/or extended using the CPDF technique. Efforts are presently underway to recode in **C++** and integrate the technique into **WaveTrain**™ as the class **CPDFScreen** to be derived

from the base class `wtPhaseScreen`.

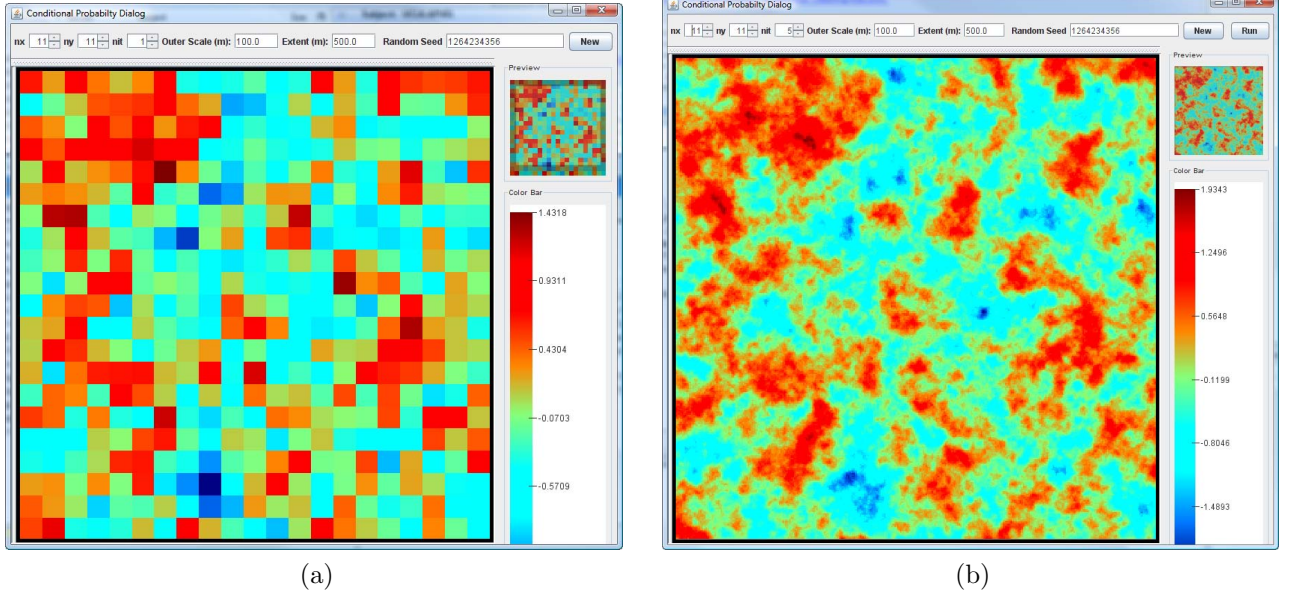


Figure 5.2: The Java-based GUI for generating phase screens based on the CPDF technique. The course resolution screen in shown in (a) and the fine resolution screen in shown in (b).

5.2.2 Closed Loop Tracking Performance

A crucial aspect of the numerical simulation of optical propagation through atmospheric turbulence is the generation of random phase screens with the correct statistics. The most popular technique used is the DFT using the computationally efficient fast Fourier transform (FFT) algorithm. It is well known that in order to adequately model the low spatial frequency content of the atmospheric disturbance, one must either generate large (much larger than the propagation grid) phase screens or “boost” the low frequency content of the random screens (Zernike boost or Sub-harmonics are two such methods). Often times an argument is made that if atmospheric tracking (tilt compensation) is implemented, the low frequency content can be ignored and the FFT technique is adequate. That argument is investigated in this study. Comparisons of relevant statistics are shown under various tracking conditions (including anisoplanatism) using random phase screens known to be lacking in low spatial frequency content (FFT) and random screens with the proper low spatial frequency content.

Using the modified FS approach described in Sec. 5.2.1, we desired to determine the point at which the low spatial frequency disturbances become important. Under the frozen flow hypothesis, the temporal tilt (Zernike 2 and 3) PSD can be expressed in terms of the spatial phase PSD and the velocity [1]

$$\Omega_{2,3}(f) = 4\pi^2 k^2 L R \int_0^1 \frac{dz}{v(z)} \int_{2\pi f_1}^{\infty} dK K \Phi_n(K/R) \frac{1 + \cos[K^2 N z(1-z)]}{\sqrt{K^2 - (2\pi f_1)^2}} |\hat{h}_{2,3}(\alpha, \beta)|^2 \quad (5.7)$$

where K is normalized spatial frequency, and $f_1 = fD/2v$, is normalized temporal frequency. For a given temporal frequency, normalized spatial frequencies below $2\pi f_1$ do not contribute to the

temporal PSD. When using phase screens with a minimum spatial frequency content of $K_{\min} > 2\pi f_1$, normalized temporal frequencies below K_{\min} are under-represented. An example temporal phase spectrum (from a wave-optics simulation) is shown in Fig. 5.3 for phase screens generated using the FFT technique and the modified FS approach. As can be seen in the plot, at low temporal

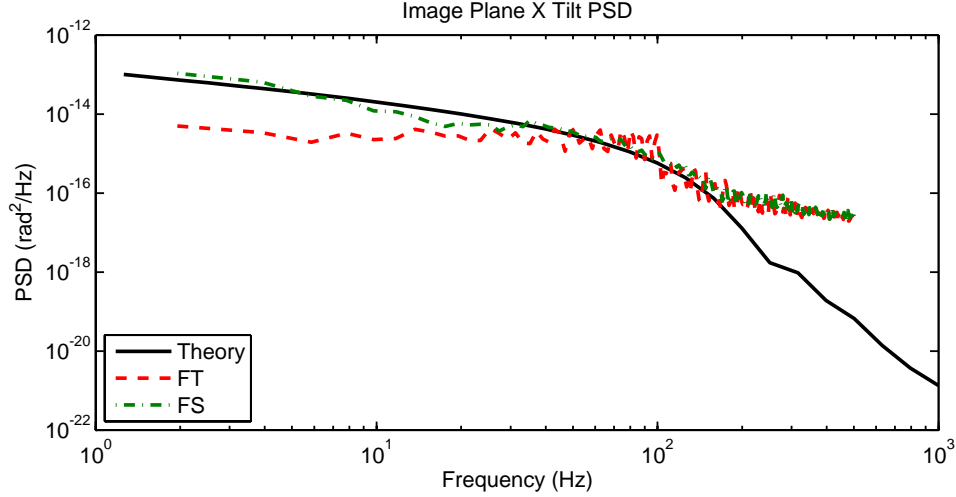


Figure 5.3: Example temporal spectra for two different wave-optics simulations each using a different technique for generating random phase disturbances.

frequencies, the power is low when compared to the theoretical PSD.

We have run a set of wave-optics simulations using **WaveTrain™ mex** systems to determine the dependence of closed-loop tracking performance on the spatial frequency content of the phase disturbances. We implemented point source tracking for a “tactical” HEL scenario [see Table 5.2]. The

Table 5.2: Simulation Parameters for closed loop tracking study

Parameter	Value
Platform Altitude	3000 m
Target Altitude	10 m
Platform Velocity	100 m/s
Target Velocity	10 m/s
Aperture Diameter	0.5 m
Wavelength	1.064 μm
C_n^2 Profile	$2 \times \text{HV}_{5/7}$
Spherical r_0	0.27 m
Rytov	0.11
Isoplanatic Angle	1.5 μrads
Greenwood Frequency	189 Hz
Tyler Frequency	28 Hz
Frame Rate	1000 Hz

first step was to verify the error rejection function of our tracker. The theoretical error rejection

function for a simple integrator with latency is

$$\text{ERJ}(f) = \left[1 + \left(\frac{f_{BW}}{f} \right)^2 - 2 \left(\frac{f_{BW}}{f} \right) \sin(2\pi f \Delta t) \right]^{-1} \quad (5.8)$$

where f_{BW} is the 3dB closed loop bandwidth, and Δt is the latency. The closed loop bandwidth and closed loop gain, β , are related by

$$\beta = 2\pi \frac{f_{BW}}{F_s} \quad (5.9)$$

where F_s is the frame rate. We set up a simple simulation to verify this form of the error rejection function. The WaveTrain™ system and the results of the error rejection test are shown in Fig. 5.4. As can be seen in the figure, the form of the error rejection function from the simulation matches

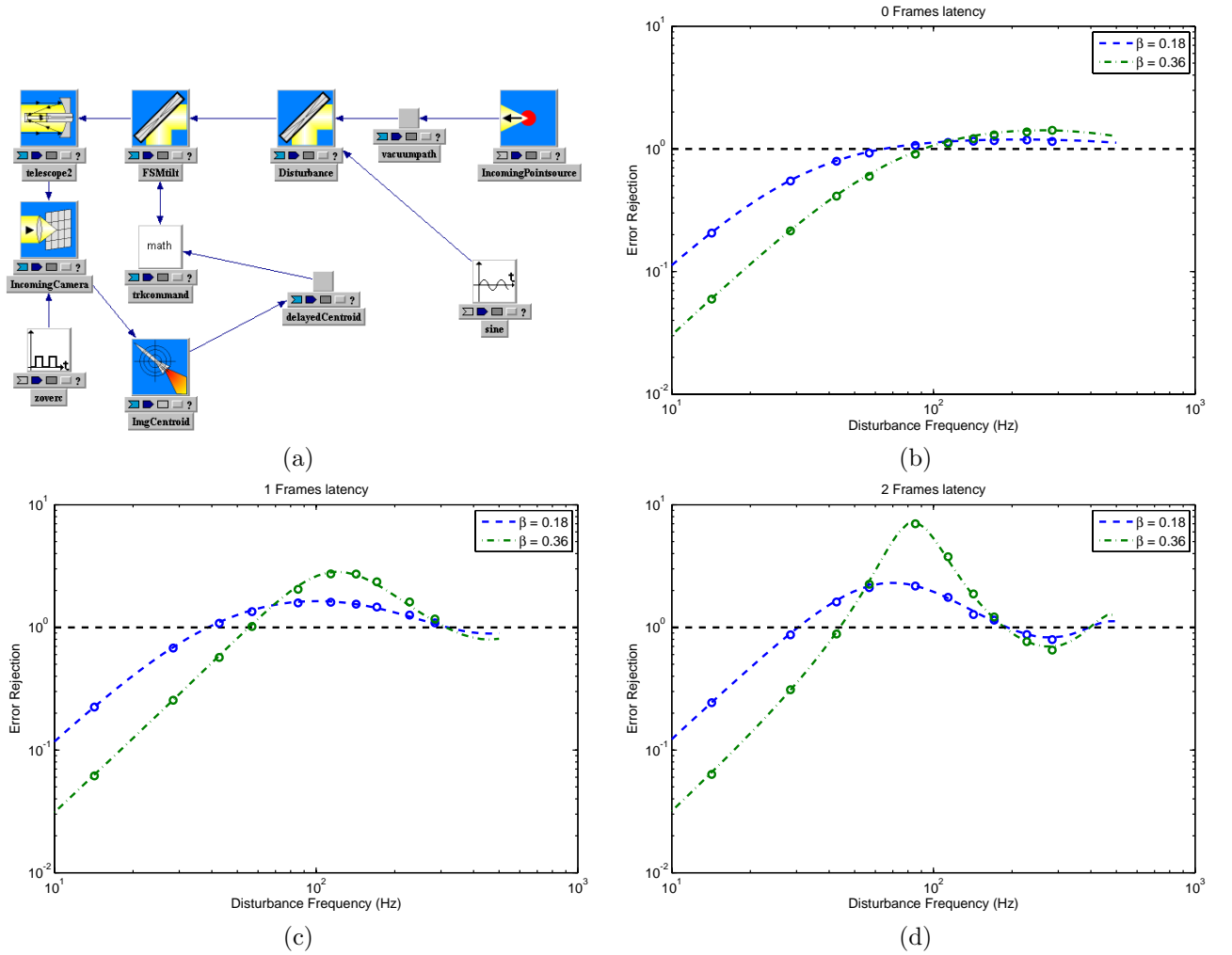


Figure 5.4: Verification of the WaveTrain™ error rejection function. (a) The WaveTrain™ system used and the error rejection test results for (a) 0 frames, (b) 1 frame, and (c) 2 frames of latency. The lines are the theoretical values [see (5.8)] and the circles are the results from the WaveTrain™ simulation.

the theoretical form from (5.8).

The simulation results for closed loop tracking are shown in Fig. 5.5 as a function of the normalized (by Tyler frequency) closed loop bandwidth. At low closed loop bandwidth (less than the Tyler

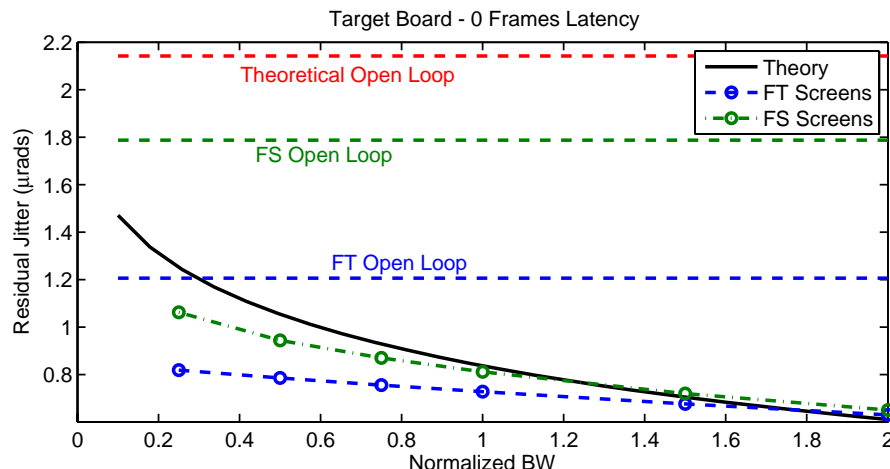


Figure 5.5: Target board residual jitter results of closed loop tracking simulation using standard FFT screens (blue circles) and modified FS screens (green circles) as compared to the theoretical values (black line).

frequency) the discrepancy between the FFT screens and the FS screens is obvious, especially for 2 frames of latency. However, as the bandwidth increases to greater than the Tyler frequency, the resulting residual jitter appears to be independent of the spatial frequency content in the random screens. In order to get more than 90% of the residual jitter predicted by the FS approach using a FFT approach, the closed loop bandwidth must be greater than the Tyler frequency.

5.2.3 Orbital Propagator

A recent addition to the Scaling for HEL and Relay Engagements (SHaRE) **MATLAB**® toolbox is the capability of generating engagement scenarios which include orbital assets. We have incorporated into SHaRE the North American Aerospace Defense Command (NORAD) SGP4 (for near-earth objects) and SDP4 (for deep-space objects) algorithms for determining satellite location and velocity in earth orbit using current NORAD two-line element (TLE) datum. This allows us to investigate the energy characteristics of a ground based laser to an orbital asset. We have conducted a study using such a simulation to demonstrate the use of the orbital propagator under a diverse set of atmospheric conditions. The ephemeris data for selected satellites is retrieved from freely released TLE satellite catalogs (www.space-track.org). The atmospheric data and satellites state vectors are then feed into a line-of-site algorithm for analysis. This determines the access times and look angles between ground sites and assets. Based on the engagement geometry, SHaRE was used to quantitatively define the open loop and closed loop characteristic of the energy at target. An example of computing satellite positions and visibility from a ground station is shown in Fig. 5.6.

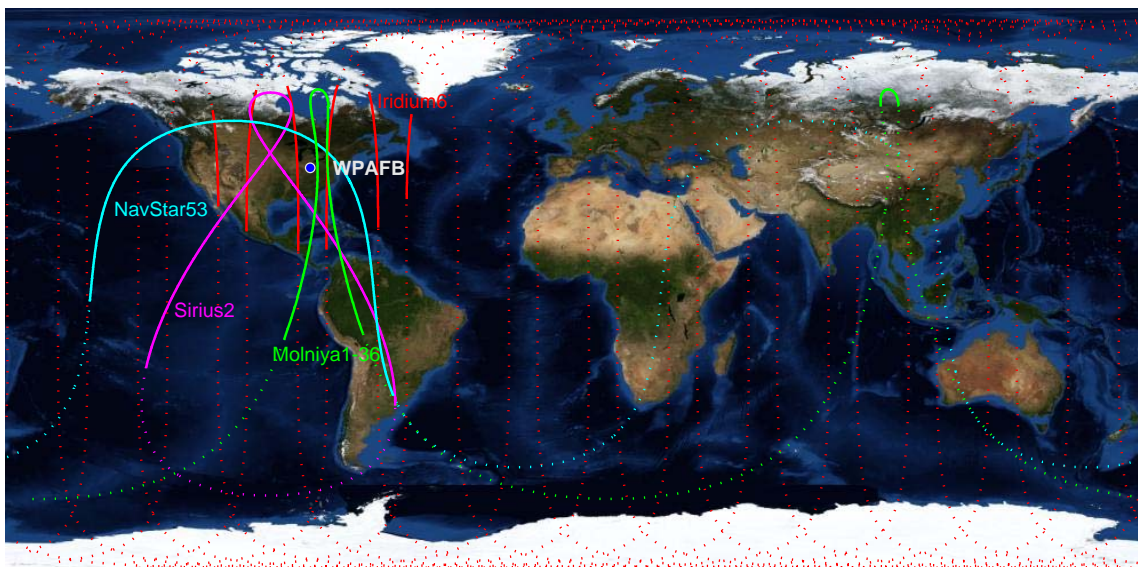


Figure 5.6: Satellite ground track and visibility from WPAFB on 10 October 2006. Solid lines represent times at which the satellite would have been visible from a ground station at WPAFB.

5.2.4 Extreme and Percentile Environmental Reference Tables Atmosphere

As a by-product of an effort to integrate the SHaRE **MATLAB**® toolbox with the Air Force Institute of Technology (AFIT) High Energy Laser End-to-End Simulation (HELEEOS), we have included AFIT's extensive Extreme and Percentile Environmental Reference Tables (ExPERT) based atmospheric parameter data into SHaRE. The ExPERT database is a joint effort by the Air Force Research Laboratory's Air Vehicles and Space Vehicles Directorates, and the Air Force Combat Climatology Center. ExPERT is a Microsoft Access database of pre-calculated climatological values for various regions—land, ocean, and upper air—as well as 408 sites worldwide. For the individual surface land sites, ExPERT allows the analyst to view monthly and hourly percentile data, duration data, and yearly minimum and maximum values for the following atmospheric variables: altimeter setting, dew point temperature, absolute humidity, relative humidity, specific humidity, temperature, wind speed, and wind speed with gusts. Percentiles for diurnal data and sky cover data are displayed as well. Also available are the percent frequency of occurrence for several “significant” weather phenomena: thunderstorms, fog, blowing snow or sand, freezing rain, hail, snow, and rain. Notably, ExPERT also enables the analyst to display the probabilities of when a particular combination of temperature and relative humidity will occur for a specific land site. Using ExPERT and the Global Aerosol Data Set (GADS), along with the High-Resolution Transmission Molecular Absorption Database (HITRAN), AFIT has generated a look-up table (LUT) for molecular and aerosol absorption and scattering, temperature, and pressure. The free parameters in the LUT available for use in ATMTTools are altitude (up to 80 kft), boundary layer altitude, wavelength (24 values), site (408 worldwide), season (summer or winter), time of day (8 periods and a daily average), and relative humidity (9 values). Fig. 5.7 shows the available locations in the ExPERT database.

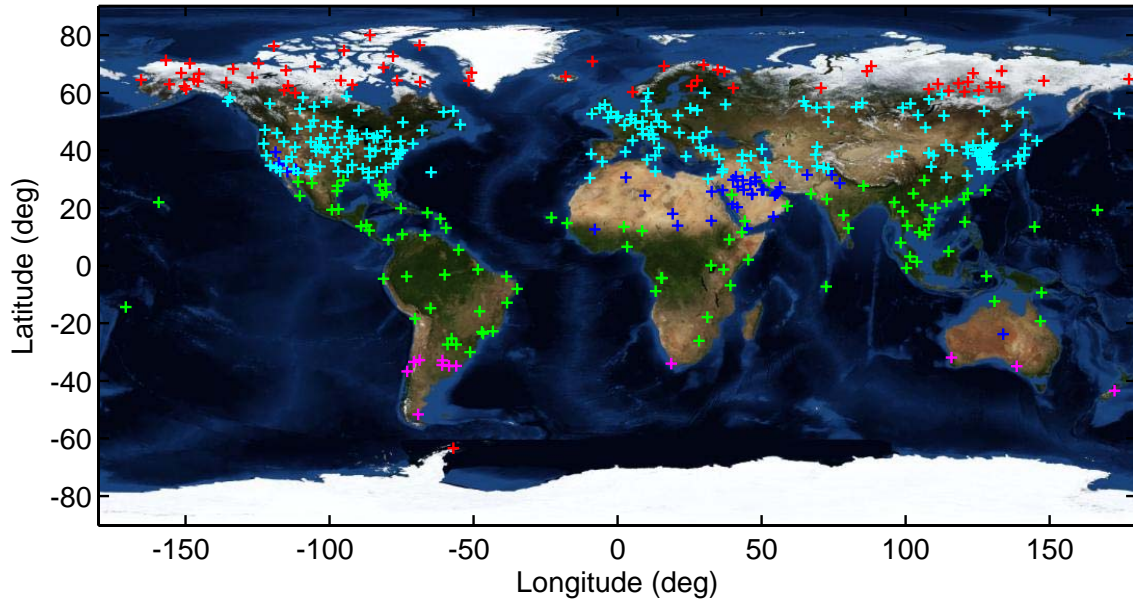


Figure 5.7: Available locations in the ExPERT database. The sites are classified into 5 categories, desert (blues), north latitudes (cyan), polar (red), south latitudes (magenta), and tropical (green).

5.2.5 Implementation of Adaptive Controller in WaveTrain™

The adaptive controller developed by UCLA was implemented in MATLAB®/Simulink® models using mex functions. In an effort to incorporate the adaptive controller in a WaveTrain™ simulation, MZA worked with UCLA graduate assistant Yutai Liu to first call the MATLAB® functions from a WaveTrain™ block via the MATLAB® engine (called an m-system) and then later to have the WaveTrain™ block directly call the functions in the C++ code underlying the mex functions. The implementation was verified by comparing the WaveTrain™ and Simulink® results.

5.2.6 Laboratory and Wave Optics Analysis of Aero-Optical Effects

Aero-optical OPD wind tunnel data taken at the University of Notre Dame (UND) was applied to a liquid crystal (LC) spatial light modulator (SLM) at the AFIT adaptive optics (AO) laboratory at Wright-Patterson Air Force Base (WPAFB). Captain Jason Schmidt (AFIT/ENG) permitted MZA to use this facility during the assembly of the MZA laboratory. The wind tunnel data was also incorporated as an OPD in a WaveTrain™ simulation. Jitter, Strehl, and wavefront sensor (WFS) slopes were analyzed. Comparisons showed that laboratory and WaveTrain™ results agreed well.

Aero-optic OPD Data

The data provided by the UND Aero-Optics Group included two runs each with the turret at 120° and 130° azimuth angles. Zernike decomposition of the OPD data on a frame-by-frame basis was completed for Zernike modes 1 to 55 (using Noll's numbering convention [2]). The PSD was calculated for each Zernike mode. Fractional power of each mode (up to Zernike 10) for each of the four runs is presented in Fig. 5.8. Behavior with respect to disturbance by Zernike mode cannot be generalized other than noting that higher order Zernike modes have more fractional power in the 130° data sets than the 120° data sets. PSDs for modes with total power greater than 5% of the

total disturbance power are presented in Fig. 5.9. For both the 120° and 130° data the disturbance power is dominant in frequencies less than or equal to 100 Hz. In the 120° data, the drop in power for frequencies greater than 100 Hz is sharper than that of the 130° data, and the variation in disturbance frequency modes for higher frequencies is more pronounced in the 130° data.

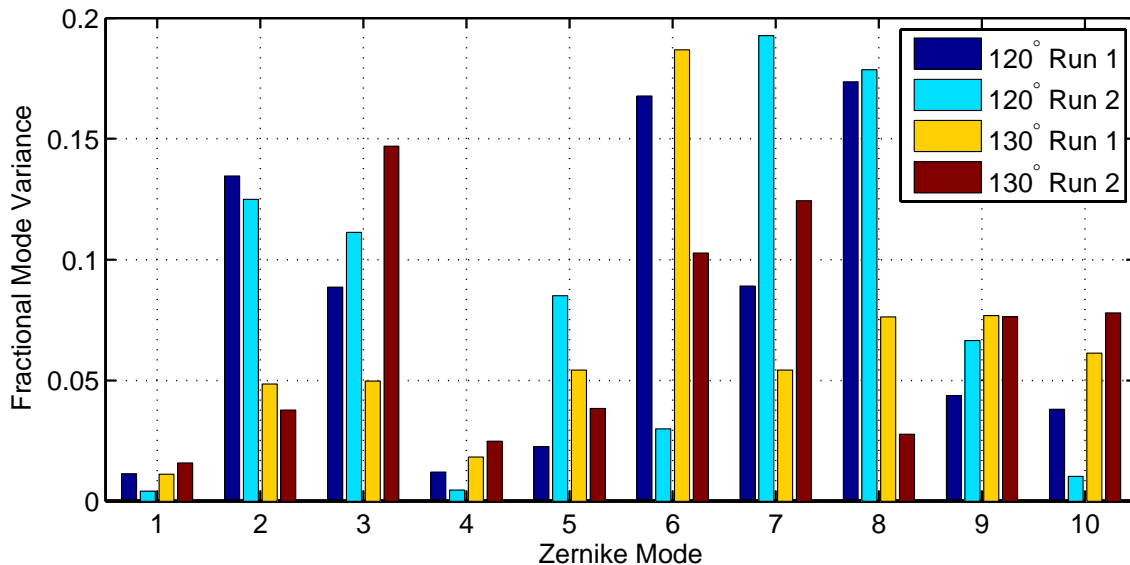


Figure 5.8: Fraction of total power in the first 10 Zernike modes for each of the data sets.

WaveTrain™ Modeling

A WaveTrain™ model for simulating the effects of propagation thorough an aero-optics disturbance was developed. The WaveTrain™ wave-optics model is a simple model which included the OPD input as its sole disturbance. Modeling parameters are shown in Table 5.3. Strehl values were calculated using a Gaussian quadrature analysis of intensity degradation. Jitter was determined as the time-variance of the centroid positions.

Table 5.3: Modeling parameters for WaveTrain™ aero-optics model

Parameter	Value
Telescope Diameter	7.55 mm
Source Wavelength	632.8 nm

Laboratory Analysis

For the experimental portion, we used AFIT's AO laboratory. The setup included a Helium:Neon (HeNe) laser at 632.8 nm, a 512×512 SLM, a 32 subaperture Shack-Hartmann WFS, and a far-field scoring camera. The illuminated portion of the SLM and WFS measured 7.55 μm across and the camera pixel spacing was 6.7 μm. The OPDs were up-sampled to a 512×512 grid, applied to the SLM, and corresponding WFS slopes and far-field camera images were recorded. For comparison, a

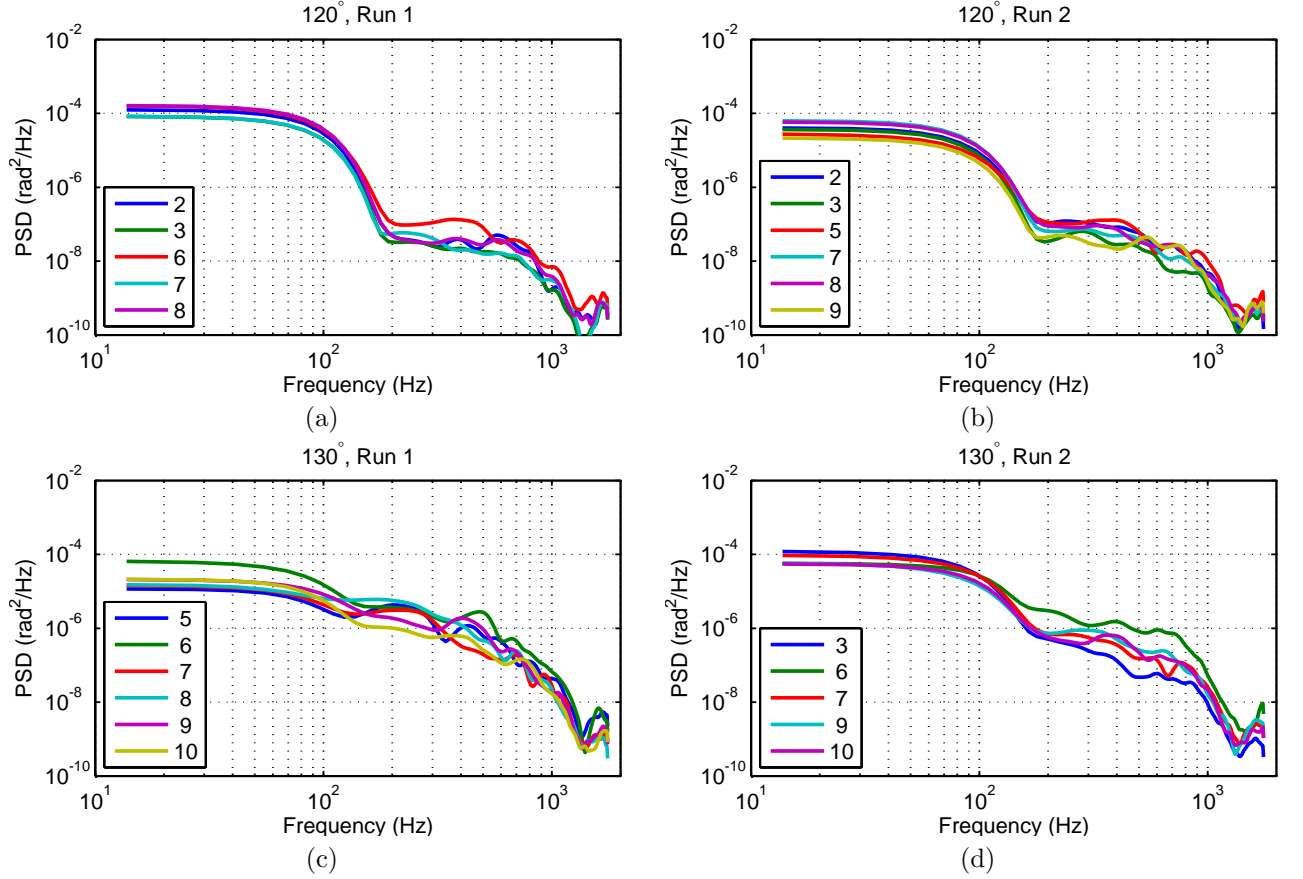


Figure 5.9: PSDs for Zernike modes which represented more than 5% of total disturbance power by data file (a) 120°, Run 1, (b) 120°, Run 2, (c) 130°, Run 1 and (d) 130°, Run 2

set of data was taken with a zero OPD applied to the SLM. The far-field images were processed by time-averaging and tilt-removed time averaging. The higher-order Strehl was calculated as the ratio of the peak of the tilt-removed, time-averaged image to the peak value of the comparison zero OPD set. The long-term Strehl values were calculated as the ratio of the peak of the time-averaged image to the peak value of the comparison set. Jitter was computed by taking the standard deviation of the centroid shift on a frame-by-frame basis. The laboratory parameters are summarized in Table 5.4. The calibration run with zero OPD data indicated a slight change in SLM behavior over time of

Table 5.4: Laboratory Parameters

Parameter	Value
Telescope Diameter	0.28 m
Source Wavelength	1 μm

use. The centroid drifts over a sequence of 450 frames. This indicates an effect of either heating or continuous voltage application. This centroid drift can be seen in Fig. 5.10.

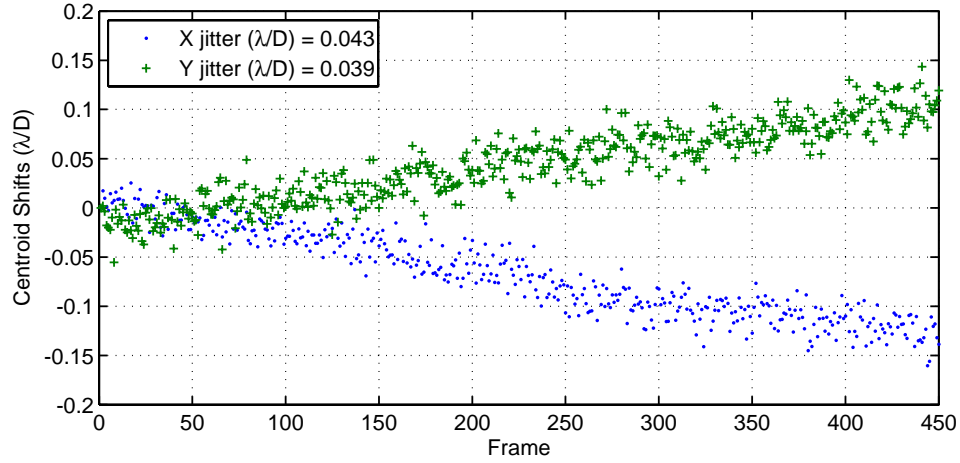


Figure 5.10: Indication of drift for SLM use over time for zero OPD run

Wavefront Sensor Comparison with Spatial Light Modulator Input

The wavefront was reconstructed from the WFS slopes and compared to the OPDs placed on the SLM. The mean-squared error (MSE) between the input OPD and the reconstructed phase was calculated on a frame-by-frame basis. The reconstructed phase from the WFS agrees very well with the OPD data when the phase variance is small (120° , Run 2). The agreement is less accurate for cases with greater disturbances, but the WFS phase variance results reflect the overall trend in the OPD variance [see Fig. 5.11]. Examples of the best match (in terms of MSE) and worst match phase reconstructions and time-average far field irradiance patterns are shown in Fig. 5.12 and Fig. 5.13.

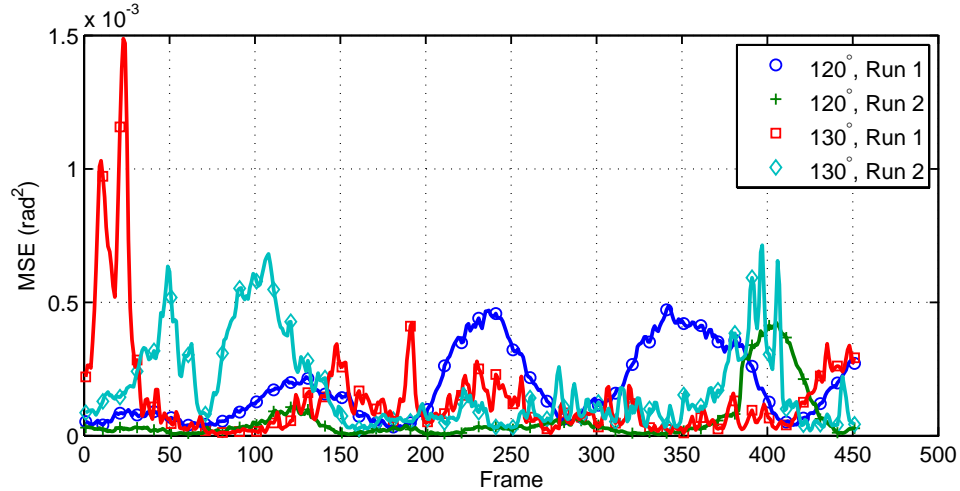


Figure 5.11: Mean squared error between the input OPD phase and the reconstructed phase from WFS slope measurements in the laboratory.

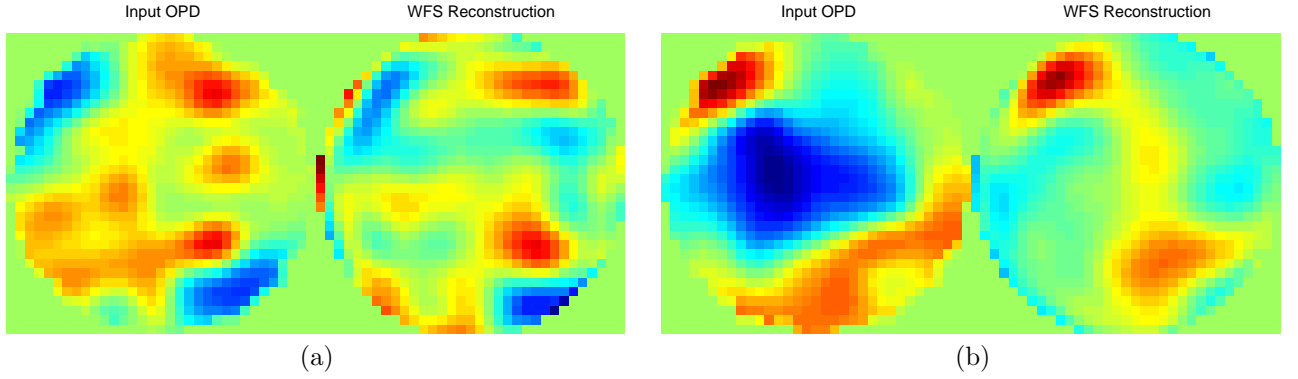


Figure 5.12: Example input and reconstructed phase maps for (a) the best match (frame 336 from 120°, Run2) and (b) the worst match (frame 23 from 130°, Run1). Even in the worst case, some of the same trends can be observed in the phase reconstruction as in the input OPD.

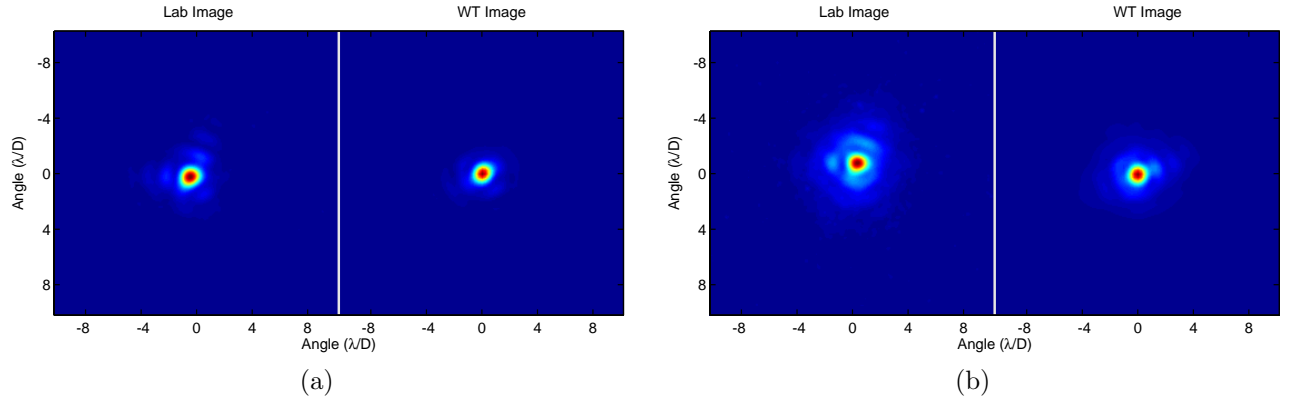


Figure 5.13: Example WaveTrain™ and laboratory measured time-averaged far field patterns for (a) 120°, Run2 and (b) 130°, Run1.

Results Summary

The WaveTrain™ results agree very well with the laboratory results and averaged images share distinctive features [see Fig. 5.13]. Strehl values show the same trends and very similar values. The jitter values are slightly higher in the laboratory than in the WaveTrain™ model. This difference can be partially explained by the SLM drift observed with the zero OPD runs. A results summary is shown in Table 5.5.

Table 5.5: Results comparison summary

Data Set	120°, Run 1	120°, Run 2	130°, Run 1	130°, Run 2
WaveTrain™ Strehl	0.21	0.59	0.31	0.24
Laboratory L.T. Strehl	0.24	0.60	0.26	0.19
Laboratory H.O. Strehl	0.25	0.61	0.25	0.19
WaveTrain™ X Jitter (λ/D)	0.0924	0.0480	0.0420	0.0238
WaveTrain™ Y Jitter (λ/D)	0.1512	0.0258	0.0219	0.0177
Laboratory X Jitter (λ/D)	0.1272	0.0904	0.1777	0.1312
Laboratory Y Jitter (λ/D)	0.1706	0.1440	0.1486	0.2091

Bibliography

- [1] C. B. Hogge and R. R. Butts, “Frequency spectra for the geometric representation of wavefront distortions due to atmospheric turbulence,” *IEEE Transactions on Antennas and Propagation*, vol. 24, no. 2, pp. 144–154, 1976.
- [2] R. J. Noll, “Zernike polynomials and atmospheric turbulence,” *J. Opt. Soc. Am.*, vol. 66, pp. 207–211, 1976.

List of Abbreviations

ABL	Airborne Laser
AFIT	Air Force Institute of Technology
AFOSR	Air Force Office of Scientific Research
AO	adaptive optics
ATK	Alliant Techsystems
CPDF	conditional probability density functions
DFT	discrete Fourier transform
ExPERT	Extreme and Percentile Environmental Reference Tables
FFT	fast Fourier transform
FS	Fourier series
GADS	Global Aerosol Data Set
HEL	high energy laser
HEL-JTO	High Energy Laser Joint Technology Office
HELEEOS	High Energy Laser End-to-End Simulation
HeNe	Helium:Neon
HITRAN	High-Resolution Transmission Molecular Absorption Database
LC	liquid crystal
LUT	look-up table
MSE	mean-squared error
MZA	MZA Associates Corporation
NORAD	North American Aerospace Defense Command
OPD	optical path difference
PSD	power spectral density
SBIR	Small Business Innovative Research
SHaRE	Scaling for HEL and Relay Engagements
SLM	spatial light modulator
TLE	two-line element
UCLA	University of California at Los Angeles
UND	University of Notre Dame
WFS	wavefront sensor
WPAFB	Wright-Patterson Air Force Base

Chapter 5

Active Contours for Tracking

GEORGIA TECH

5.1 Introduction

An active contour approach driven by ideas from knowledge-based segmentation was developed for missile tracking through deep turbulence. Prior work on laser-guided target tracking for missiles has focused on understanding the source of jitter and reducing jitter through controller design for the optical system. Although effective plant and controller design lead to performance improvements, turbulence effects are a consistent source of noise arising from the image processing not modelled within the physics underlying tilt stabilization, which is what an effective tilt controller design typically corrects for.

Our research has shown how geometric active contours driven by Bayesian statistical techniques may be used in order to dynamically track missiles through deep turbulence.

We can summarize our contributions as follows:

- All of the smoothing we do for the posteriors is based on active contour methods (anisotropic image enhancement). Thus each isophote (equal probability contour) is moving according to a standard curve evolution flow.
- Active contours without edges (region-based active contours) appear in the estimation of the gain factor for separating the foreground from the background classes.
- Active contours are used for tip tracking.

We now briefly summarize some key aspects of our work in the next sections.

5.2 Bayesian Tracking

The active contours are driven by a Bayesian estimation technique as follows: Suppose that each threshold graylevel belongs to a particular class, the image to segment consists of M classes of graylevels $C = \{1, \dots, M\}$, and that each class $c \in C$ is associated with a mean pixel intensity μ_c and standard deviation σ_c . The goal of the segmentation process is to map each pixel intensity into a class. A pixel intensity measurement v_i is a random variable with known distribution, independent of the other pixels in the image domain. Given prior knowledge of the image statistics, the probability of a pixel intensity being assigned to a particular class is given by Bayes' Rule,

$$\Pr(c_i = c | v_i = v) = \frac{\Pr(v_i = v | c_i = c) \Pr(c_i = c)}{\sum_{\gamma} \Pr(v_i = v | c_i = \gamma) \Pr(c_i = \gamma)}, \quad (5.1)$$

where the probability $\Pr(v_i = v|c_i = c)$ is assumed to have a Gaussian distribution¹,

$$\Pr(v_i = v|c_i = c) = \frac{1}{\sqrt{2\pi}\sigma_c} \exp\left\{-\frac{1}{2} \frac{(v - \mu_c)^2}{\sigma_c^2}\right\}, \quad (5.2)$$

with (μ_c, σ_c) the mean and standard deviation corresponding to the class $c \in C$. The posterior probabilities from equation (4.1) are calculated for each class, then smoothed and normalized to obtain $\widehat{\Pr}$. The pixel i is assigned to the class with the maximal smoothed posterior probability,

$$c_i^* = \arg \max_{c \in C} \widehat{\Pr}(c_i = c|v_i = v). \quad (5.3)$$

Computing the posterior probabilities begins with the assumption of known image statistics, i.e., the prior probabilities $\Pr(c_i = c)$ are needed, as are the mean and standard deviations corresponding to the classes C . Initially the probabilities $\Pr(c_i = c)$ are assumed to be homogeneous. After the first image, the priors are set to be the posteriors from the previous time step. The means μ_c and standard deviations σ_c for the classes $c \in C$ are updated from their previous state according to the computed statistics of the current segmentation.

Implementing Bayes' Rule for a sequence of images without smoothing of the posteriors will tend to result in convergence to a fixed steady state segmentation, potentially incorrect. Such a convergence is undesirable when dealing with moving imagery, as is the case discussed here. To prevent the segmentation process from converging, smoothing of the posteriors is performed. The smoothing process, performed prior to the MAP classification, has the additional benefit of removing noise.

5.3 Background on Curve Evolution

One can think of an image as a map $I : \mathcal{D} \rightarrow \mathcal{C}$, i.e., to any point \mathbf{x} in the domain \mathcal{D} , I associates a "color" $I(\mathbf{x})$ in a color space \mathcal{C} . For ease of presentation we will mainly restrict ourselves to the case of a two-dimensional gray scale image which we can think of as a function from a domain $\mathcal{D} = [0, 1] \times [0, 1] \subset \mathbb{R}^2$ to the unit interval $\mathcal{C} = [0, 1]$.

The algorithms all involve solving the initial value problem for some PDE for a given amount of time. The solution to this PDE can be either the image itself at different stages of modification, or some other object (such as a closed curve delineating object boundaries) whose evolution is driven by the image.

For example, introducing an artificial time t , the image can be deformed according to

$$\frac{\partial I}{\partial t} = \mathcal{F}[I], \quad (5.4)$$

where $I(\mathbf{x}, t) : \mathcal{D} \times [0, T] \rightarrow \mathcal{C}$ is the evolving image, \mathcal{F} is an operator which characterizes the given algorithm, and the initial condition is the input image I_0 . The processed image is the solution $I(\mathbf{x}, t)$ of the differential equation at time t . The operator \mathcal{F} usually is a differential operator, although its dependence on I may also be nonlocal.

Similarly, one can evolve a closed curve $\Gamma \subset \mathcal{D}$ representing the boundaries of some planar shape (Γ need not be connected and could have several components). In this case, the operator \mathcal{F} specifies the normal velocity of the curve that it deforms. In many cases this normal velocity is a function of the curvature κ of Γ , and of the image I evaluated on Γ . A flow of the form

$$\frac{\partial \Gamma}{\partial t} = \mathcal{F}(I, \kappa) \mathbf{N} \quad (5.5)$$

is obtained, where \mathbf{N} is the unit normal to the curve Γ .

¹Alternative distributions better suited to the image statistics may be picked for the classes. A more representative distribution improves the segmentation process.

Very often, the deformation is obtained as the steepest descent for some energy functional. For example, the energy

$$\mathcal{E}(I) = \frac{1}{2} \int \|\nabla I\|^2 \, dx dy \quad (5.6)$$

and its associated steepest descent, the heat equation,

$$\frac{\partial I}{\partial t} = \Delta I \quad (5.7)$$

correspond to the classical Gaussian smoothing.

The use of PDEs allows for the modelling of the crucial but poorly understood interactions between top-down and bottom-up vision. In a variational framework, for example, an energy \mathcal{E} is defined globally while the corresponding operator \mathcal{F} will influence the image locally. Algorithms defined in terms of PDEs treat images as continuous rather than discrete objects. This simplifies the formalism, which becomes grid independent. On the other hand models based on nonlinear PDEs may be much harder to analyze and implement rigorously.

5.4 Geometric Active Contours

For geometric active contours, one deforms the active contour Γ by a velocity which is essentially defined by a curvature term, and a constant inflationary term weighted by a stopping function W . By formulating everything in terms of quantities which are invariant under reparametrization (such as the curvature and normal velocity of Γ) one obtains an algorithm which does not depend on the parametrization of the contour. In particular, it can be implemented using level sets.

More specifically, a simple geometric model is given by

$$V = W(\mathbf{x})(\kappa + c), \quad (5.8)$$

where both the velocity V and the curvature κ are measured using the inward normal \mathbf{N} for Γ . Here, as previously, W is small at edges and large everywhere else, and c is a constant, called the *inflationary parameter*. When c is positive, it helps push the contour through concavities, and can speed up the segmentation process. When it is negative, it allows expanding “bubbles,” i.e., contours which expand rather than contract to the desired boundaries. We should note that there is no canonical choice for the constant c , which has to be determined experimentally.

In practice Γ is deformed using the Osher-Sethian level set method. One represents the curve Γ_t as the zero level set of a function $\Phi : \mathcal{D} \times \mathbb{R}^+ \rightarrow \mathbb{R}$,

$$\Gamma^t = \{\mathbf{x} \in \mathcal{D} : \Phi(\mathbf{x}, t) = 0\}. \quad (5.9)$$

For a given normal velocity field, the defining function Φ is then the solution of the Hamilton-Jacobi equation

$$\frac{\partial \Phi}{\partial t} + V \|\nabla \Phi\| = 0$$

which can be analyzed using viscosity theory.

Geometric active contours have the advantage that they allow for topological changes (splitting and merging) of the active contour Γ . The main problem with this model is that the desired edges are not steady states for the flow 4.8. The effect of the factor $W(\mathbf{x})$ is merely to slow the evolution of Γ_t down as it approaches an edge, but it is not the case that the Γ_t will eventually converge to anything like the sought-for edge as $t \rightarrow \infty$. Some kind of artificial intervention is required to stop the evolution when Γ_t is close to an edge.

5.4.1 Conformal (Geodesic) Active Contours

For conformal active contours, one defines a Riemannian metric g^W on \mathfrak{D} from a given image $I : \mathfrak{D} \rightarrow \mathbb{R}$, by conformally changing the standard Euclidean metric to,

$$g^W = W(\mathbf{x})^2 \|\mathrm{d}\mathbf{x}\|^2. \quad (5.10)$$

The length of a curve in this metric is

$$\mathcal{L}^W(\Gamma) = \int_{\Gamma} W(\Gamma(s)) \, \mathrm{d}s. \quad (5.11)$$

Curves which minimize this length will prefer to be in regions where W is small, which is exactly where one would expect to find the edges. So, to find edges, one should minimize the W -weighted length of a closed curve Γ , rather than some “energy” of Γ (which depends on a parametrization of the curve).

To minimize $\mathcal{L}^W(\Gamma)$, one computes a gradient flow in the L^2 sense. Since the first variation of this length functional is given by

$$\frac{\mathrm{d}\mathcal{L}^W(\Gamma)}{\mathrm{d}t} = - \int_{\Gamma} V \{ W\kappa - \mathbf{N} \cdot \nabla W \} \, \mathrm{d}s,$$

where V is the normal velocity measured in the Euclidean metric, and \mathbf{N} is the Euclidean unit normal, the corresponding L^2 gradient flow is

$$V_{\text{conf}} = W\kappa - \mathbf{N} \cdot \nabla W. \quad (5.12)$$

Contemplation of the conformal active contours leads to another interpretation of the concept “edge.” Using the landscape metaphor one can describe the graph of W as a plateau (where $|\nabla W|$ is small) in which a canyon has been carved (where $|\nabla W|$ is large). The edge is to be found at the bottom of the canyon. Now if W is a Morse function, then one expects the “bottom of the canyon” to consist of local minima of W alternated by saddle points. The saddle points are connected to the minima by their unstable manifolds for the gradient flow of W (the ODE $\mathbf{x}' = -\nabla W(\mathbf{x})$.) Together these unstable manifolds form one or more closed curves which one may regard as the edges which are to be found.

5.5 Region-Based Active Contours

We can easily include statistic globally based terms in our framework. This is derived from the following type problem:

$$\text{minimize } \int_{\text{interior } \mathcal{C}} f_1 \mathrm{d}\mathbf{x} + \int_{\text{exterior } \mathcal{C}} f_2 \mathrm{d}\mathbf{x} \quad (5.13)$$

for globally defined functions f_1 and f_2 . For example, to separate means, we define $u = S_u/A_u$, $w = S_w/A_w$, and

$$\begin{aligned} S_u &= \int_{R^u} I \, \mathrm{d}\mathbf{x} & A_u &= \int_{R^u} \mathrm{d}\mathbf{x} \\ S_w &= \int_{R^w} I \, \mathrm{d}\mathbf{x} & A_w &= \int_{R^w} \mathrm{d}\mathbf{x}, \end{aligned}$$

and R^u and R^w denote the domains inside and outside the curve respectively. Computing the first variation results in the following gradient flow for separating the means of regions

$$\Gamma_t = (u - w) \left(\frac{I - u}{A_u} + \frac{I - w}{A_w} \right) \mathbf{N}. \quad (5.14)$$

5.6 Papers of Allen Tannenbaum Supported by MRI-HEL

1. "Optimal mass transport for registration and warping" (with S. Haker and L. Zhu), *Int. Journal Computer Vision* **60** (2004), pp. 225-240.
2. "Area-based medial axis of planar curves," (with S. Betelu, M. Niethammer, and G. Sapiro), *Int. Journal Computer Vision* **60** (2004), 203-224.
3. "Flux driven automatic centerline extraction" (with S. Bouix and K. Siddiqi), *Medical Image Analysis* **9** (2005), 209-221.
4. "Dynamic active contours for visual tracking" (with S. Angenent and M. Niethammer), *IEEE Trans. Automatic Control* **51** (2006), pp. 562-579.
5. "On the evolution of closed curves by means of vector distance functions" (with M. Niethammer and P. Vela), *Int. Journal Computer Vision* **65** (2005), pp. 5-27.
6. "Detecting simple points in higher dimensions" (with M. Niethammer, W. Kalies, and K. Mischaikow), *IEEE Image Processing* **15** (2006), pp. 2462- 2469.
7. "Development and testing of highly autonomous unmanned aerial vehicles" (with J. Ha, E. Johnson, and A. Proctor), *AIAA Journal of Aerospace Computing, Information, and Communication* **1** (2004), No. 12, pp. 485-501.
8. "Mathematical methods in medical imaging" (with S. Angenent and E. Pichon), *Bull. Amer. Math. Soc. (N.S.)* **43** (2006), pp. 365-396.
9. "A method for prediction and estimation of large-amplitude optical flows - an extended Kalman filtering approach" (with O. Michailovich), *Engineering Computations* **23** (2006), pp. 503-514.
10. "A generic framework for tracking using particle filter with dynamic shape prior" (with Y. Rathi), *IEEE Trans. Image Processing* **16** (2007), pp. 1370-1382 .
11. "Multiscale 3D shape representation and segmentation using spherical wavelets" (with D. Nain, S. Haker, A. Bobick), *IEEE Trans. Medical Imaging* **26** (2007), pp. 598-618.
12. "Knowledge-based segmentation for tracking through deep turbulence" (with P. Vela, M. Niethammer, G. Pryor, R. Butts, and D. Washburn), to appear in *IEEE Trans. Control Technology*, 2007.
13. "Distribution metrics and image segmentation" (with T. Georgiou, O. Michailovich, Y. Rathi), to appear in *Linear Algebra and Its Applications*, 2007.
14. "An image morphing technique based on optimal mass preserving mapping" (with L. Zhu, Y. Yang, and S. Haker), *IEEE Trans. Image Processing* **16** (2007), 1481-1495.
15. "Tracking deforming objects using particle filtering for geometric active contours" (with Y. Rathi, N. Vaswani, A. Yezzi), *IEEE PAMI* **29** (2007), pp. 1470-1475.
16. "Finsler active contours" (with E. Pichon and J. Melonakos), to appear in *IEEE PAMI*.
17. "Image segmentation using active contours driven by information-based criteria" (with O. Michailovich, Y. Rathi), to appear in *IEEE Trans. Image Processing*.
18. "A framework for image segmentation using shape models and kernel space shape priors" (with S. Dambreville and Y. Rathi), to appear in *PAMI*.
19. "Fast approximation of smooth functions from samples of partial derivatives with applications to phase unwrapping" (with O. Michailovich), submitted for publication to *IEEE Signal Processing*.

20. "Blind deconvolution of images: parametric inverse filtering approach" (with O. Michailovich), submitted to *IEEE Trans. Image Processing*.
21. "Segmentation of tracking sequences using dynamically updated adaptive learning" (with O. Michailovich and N. Vaswani), submitted to *IEEE Trans. on Image Processing*.
22. "Dynamic denoising of tracking sequences of SAR data" (with O. Michailovich), submitted for publication to *Engineering Applications*.
23. "PF-MT (Particle Filter with Mode Tracker) with an interpolation effective basis for tracking local contour deformations" (with N. Vaswani, Y. Rathi, and A. Yezzi), to appear in *IEEE Trans. Image Processing*.
24. "Advanced nonlinear registration algorithms for image fusion" (with S. Warfield *et al*), in *Brain Mapping: The Methods, Second Edition* edited by Arthur Toga and John Mazziotta, Academic Press, pages 661-690, 2004.
25. "Stochastic crystalline flows" (with G. Ben-Arous and Ofer Zeitouni), in *Mathematical Systems Theory in Biology, Communications, Computation, and Finance* edited by J. Rosenthal and D. Gilliam, IMA Volumes in Mathematics and Its Applications, volume 134, pages 41-63, Springer, New York, 2004.
26. "On a stochastic model of geometric snakes" (with D. Nain, G. Unal, A. Yezzi, and O. Zeitouni), *Mathematical Methods in Computer Vision: A Handbook*, edited by O. Faugeras and N. Paragios, Springer-Verlag, 2005.
27. "Curve shortening and interacting particle systems" (with S. Angenent, A. Yezzi, and O. Zeitouni), in *Statistics and Analysis of Shapes* edited by Hamid Krim and A. Yezzi, Birkhauser, 2006, pages 303-313.
28. "Medial axis computation and evolution" (with S. Bouix, K. Siddiqi, and S. Zucker), in *Statistics and Analysis of Shapes* edited by Hamid Krim and A. Yezzi, Birkhauser, 2006, pages 1-29.
29. "A shape-based approach to robust image segmentation" (with S. Dambreville and Y. Rathi), in *Image Analysis and Recognition*, Lecture Notes in Computer Science **4141** (2006), pp. 173-183.
30. "Flux driven fly-throughs," *CVPR*, 2004.
31. "A Stokes flow based boundary integral formulation for measuring crosssections of two-dimensional tubular structures," (with M. Niethammer and E. Pichon), *ICIP*, 2004.
32. "Algorithms for stochastic approximations of curvature flows" (with G. Ben-Arous, N. Shimkin, G. Unal, and O. Zeitouni), *ICIP*, 2003.
33. "Dynamic level sets for visual tracking" (with M. Niethammer), *IEEE Conference on Decision and Control*, 2003.
34. "Statistically based surface evolution method for medical image segmentation: presentation and validation" (with E. Pichon and R. Kikinis), *MICCAI*, 2003. (Based student presentation award.)
35. "Active contours and optical flow for automatic tracking of flying vehicles" (with J. Ha, C. Alvino, G. Pryor, E. Johnson), *American Control Conference*, 2004.
36. "Image interpolation based on optimal mass preserving maps" (with L. Zhu), *Proceedings of ISBI*, 2004.
37. "Flux driven fly-throughs" (with S. Bouix and K. Siddiqi) *Proceedings of CVPR*, 2003.
38. "Dynamic geodesic snakes" (with M. Niethammer), in *Proceedings of CVPR*, 2004.

39. “Knowledge-based 3D segmentation and reconstruction of left coronary arteries using CT images” (with D. Giddens and Y. Yang), *EMBS04*, 2004.
40. “Flow patterns and wall shear stress distributions at atherosclerotic-prone sites in a human left coronary artery-an exploration using combined methods of CT and computational fluid dynamics” (with S. Jin, Y. Yang, J. Oshinski, A. Tannenbaum, J. Gruden, and D. Giddens), *EMBS04*, 2004.
41. “Image morphing based on mutual information and optimal mass transport” (with L. Zhu), *Proceedings of ICIP*, 2004.
42. “Automatic tracking of flying vehicles using geodesic snakes and Kalman filtering” (with A. Betser and P. Vela), *IEEE CDC*, 2004.
43. “Flying in formation using a pursuit guidance algorithm” (with A. Betser, G. Pryor, and P. Vela), *American Control Conference*, 2005.
44. “Tracking moving and deforming shapes using a particle filter” (with Y. Rathi, N. Vaswani, A. Yezzi), *CVPR*, 2005.
45. “Affine surface evolution for 3D segmentation” (with Y. Rathi, P. Olver, G. Sapiro), *SPIE*, 2006.
46. “Pattern detection and image segmentation with anisotropic conformal factors” (with E. Pichon), *ICIP*, 2005.
47. “Segmentation of blood vessels from CT scans: a topological approach” (with A. Szymczak and K. Mischaikow), *SPIE*, 2005.
48. “Geometric observers for dynamically evolving curves” (with M. Niethammer and P. Vela), *IEEE CDC*, 2005.
49. “Multigrid methods for the computation of L^1 optical flow” (with C. Alvino, C. Curry, and A. Yezzi), *ICIP*, 2005.
50. “Shape analysis of structures using spherical wavelets” (with S. Haker and D. Nain), *Proceedings of MICCAI*, 2005.
51. “Affine surface evolution for 3D segmentation” (with Y. Rathi, P. Olver, G. Sapiro), *Proceedings of SPIE*, 2006.
52. “Tracking in clutter and effects of thermal blooming on HEL beams” (with M. Belenkii, V. Rye, O. Michailovich, and D. Washburn), *Proceedings of SPIE*, Vol. 5895, Sept., 2005.
53. “Deconvolution of medical ultrasound images via parametrized inverse filtering” (with O. Michailovich), *Proceedings of IEEE ISBI06*, 2006.
54. “Particle filters for infinite (or large) dimensional state spaces” (with Y. Rathi, N. Vaswani, and A. Yezzi), *Proceedings of IEEE ICASSP*, 2006.
55. “Shape-based approach to robust image segmentation using kernel PCA” (with S. Dambreville), *Proceedings of CVPR*, 2006.
56. “Time-varying finite dimensional basis for tracking contour deformations” (with with Y. Rathi, N. Vaswani, and A. Yezzi), *Proceedings of CDC*, 2006.
57. “Tracking deformable objects with unscented Kalman filtering and geometric active contours ” (with S. Dambreville, and Y. Rathi), *American Control Conference*, 2006. (O. Hugo Schuck Award for Best Paper.)

58. “Nonlinear shape prior from Kernel space for geometric active contours” (with S. Dambreville, Y. Rath), *IS&T/SPIE Symposium on Electronic Imaging*, 2006.
59. “Shape-driven surface segmentation using spherical wavelets” (with D. Nain, S. Haker), *MICCAI*, 2006. (Best student paper award.)
60. “Comparative analysis of kernel methods for statistical shape learning” (with Y. Rath and S. Dambreville), *CVAMIA’06*, LNCS **4241**, pages 96-107, 2006.
61. “Seeing the unseen: Segmenting with distributions” (with Y. Rath and O. Michailovich), *Proceedings of SIP Conference*, 2006.
62. “Hybrid geodesic region-based curve evolutions for image segmentation” (with S. Lawton and D. Nain), *Proceedings of SPIE*, 2007.
63. “Segmenting images on a tensor manifold” (with O. Michailovich and Y. Rath), *CVPR’07*.
64. “Multigrid optimal transport for image registration and morphing” (with T. ur-Rehman), *Proceedings of SPIE*, 2007.
65. “Graph cut segmentation with nonlinear shape priors” (with J. Malcolm and Y. Rath), *ICIP’07*.
66. “Parametric segmentation using active contours and thresholding” (with S. Dambreville, M. Niethammer, A. Yezzi), *Signal and Image Processing’07*, 2007.
67. “GPU implementations of multigrid optimal transport” (with T. ur-Rehman, G. Pryor), *BMVC’07*, 2007.
68. “Layered active contours for tracking” (with G. Pryor, P. Vela, J. Rehg), *BMVC’07*, 2007.
69. “Finlser level set segmentation in oriented domains” (with V. Mohan and J. Melonakos), *BMVC’07*, 2007.
70. “Tracking through clutter using graph cuts” (with J. Malcolm and Y. Rath), *BMVC’07*, 2007.

5.7 Students Supported

1. Marc Niethammer (PhD; now assistant professor at UNC)
2. Eric Pichon (PhD; now project manager at General Electric)
3. Patricio Vela (postdoc; now assistant professor at Georgia Tech)

Appendix A

Personnel Supported

UCLA

Faculty: Professors Steve Gibson, Tsu-Chin Tsao, Robert M'Closkey

Students: Behnam Javanmardi, Yu-Tai Liu, Salman Monirabbasi, Pawel Orzechowski, Nestor Perez

Post Doctoral Scholars: Dr. Neil Chen, Dr. Byung-Sub Kim, Dr. Yen-Cheng Chen

Georgia Tech

Faculty: Professor Allen Tannenbaum

Students: Marc Niethammer, Gallagher Pryor, Andrew Stein, Eric Pichon

Post Doctoral Scholar: Patricio Vela

Post Doctoral Scholar: Patricio Vela

Michigan Tech

Faculty: Professors Michael Roggemann and Timothy Schulz

Students: Baoyong Liu, Ron Kazito, Yanchai Zhang, Aleksandr Sergeev, Nate Hart

Post Doctoral Scholar: Dr. Al Koivonen

ATK Mission Research Corporation

Dr. Matthew Whiteley, Dr. Eric Magee, Dr. Byron Welsh

Tempest Technoligies

Dr. Ben Fitzpatrick, Dr. Yun Wang, Dr. Li Liu

Trex Enterprises

Dr. Mikhael Belenk'ii, Dr. Vincent Rye

MZA Associates Corporation

Rebecca Beauchamp

Beulah Biggs

R. Russell Butts

Kavita Chand

Richard Drye

Eric Magee

Justin Mansell

Morris Maynard

Robert Pruas

Brent Strickler

Joe Riley

Richard St. John

Robert Suizu

Matthew Whiteley